An Iron-Calcium-Miro Axis Influences Parkinson's Risk and Neurodegeneration

Vinita Bharat[1], Roeland Vanhauwaert[1], Li Li[1], Colin M. Muir[2,3], Aarooran Sivakumaran Durairaj[1], Sujyoti Chandra[1], Yann Le Guen[4,5], Pawan Nandakishore[6], Chung-Han Hsieh[1], Stefano E. Rensi[7], Russ B. Altman[7], Michael D. Greicius[4], Liang Feng[2], and Xinnan Wang[1]*

Affiliations:
1. Department of Neurosurgery, Stanford University School of Medicine, Stanford, CA94305, USA;
2. Department of Molecular and Cellular Physiology, Stanford University School of Medicine, Stanford, CA94305, USA;
3. Graduate Program of Molecular and Cellular Physiology, Stanford University School of Medicine, Stanford, CA94305, USA;
4. Department of Neurology and Neurological Sciences, Stanford University School of Medicine, Stanford, CA94305, USA;
5. Institut du Cerveau - Paris Brain Institute - ICM, 75013, Paris, France;
6. Vroom Inc., Houston, TX77042, USA;
7. Department of Bioengineering, Stanford University, Stanford, CA94305, USA.

* Correspondence: xinnanw@stanford.edu

Summary
Genetic backgrounds and risk factors among individuals with Parkinson's disease (PD) are highly heterogenous, limiting our ability to effectively detect and treat PD. Here we connect several potential PD risk genes and elements to one biological pathway. Elevation of Fe^{2+}-levels causes Ca^{2+}-overflow into the mitochondria, through an interaction of Fe^{2+} with mitochondrial calcium uniporter (MCU), the Ca^{2+}-import channel in the inner mitochondrial membrane, and resultant MCU oligomerization. This mechanism acts in PD neuron models and postmortem brains. Miro, a Ca^{2+}-binding protein, functions downstream of Ca^{2+}-dysregulation, and holds promise to classify PD status and monitor drug efficacy in human blood cells. Polygenetic enrichment of rare, non-synonymous variants in this iron-calcium-Miro axis influences PD risk. This axis can be targeted by multiple ways to prevent neurodegeneration in PD models. Our results show a linear pathway linking several PD risk factors, which can be leveraged for genetic counseling, risk evaluation, and therapeutic strategies.

Introduction

Parkinson's disease (PD) is a leading cause of disability, afflicting the aging population. The dopamine (DA)-producing neurons in the substantia nigra are the first to die in PD patients. A bottleneck that hinders our ability to effectively detect and treat PD may be the presence of highly heterogenous genetic backgrounds and risk factors among different patients. More than 90% of the PD cases are considered sporadic with no known causal mutations. Genome-wide association studies (GWAS) have identified over 90 risk loci (Diaz-Ortiz et al., 2022). Functional studies on known causal genes of familial patients and from cellular and animal PD models have pointed to

multiple "cellular risk elements", such as mitochondrial damage, lysosomal dysfunction, immune system activation, neuronal calcium mishandling, and iron accumulation (Angelova et al., 2020; Apicco et al., 2021; Belaidi and Bush, 2016; Buttner et al., 2013; Kim et al., 2020; Lee et al., 2018; Surmeier et al., 2017; Tabata et al., 2018; Verma et al., 2017; Vuuren et al., 2020). These distinct genetic and cellular risk factors may confer individual heterogeneity in disease onset and suggest that there are networks and pathways linking these "hubs" in disease pathogenesis. Identifying their connections could be crucial for finding a cure for PD.

Mitochondria are the center of cellular metabolism and communication. Ions such as calcium and iron, are not only essential for diverse mitochondrial functions but can be stored inside the mitochondria to maintain cellular ionic homeostasis. Ion channels in the plasma and mitochondrial membranes coordinate for ion uptake, transport, and storage. For example, calcium ions enter the cell via voltage- or ligand-gated calcium channels across the cell surface. Inside the cell, they are taken up by mitochondria through the outer mitochondrial membrane (OMM) channel, VDAC, and the inner mitochondrial membrane (IMM) channel, mitochondrial calcium uniporter (MCU) (Baughman et al., 2011), and extruded into the cytosol through the IMM transporter, NCLX (Palty et al., 2010). MCU is a multimeric holocomplex consisting of additional regulatory subunits, such as essential MCU regulator (EMRE), mitochondrial calcium uptake 1 (MICU1), MICU2, and MCUb (Fan et al., 2018; Fan et al., 2020; Lambert et al., 2019). Channels complementary to these major mitochondrial calcium channels also exist (Patron et al., 2022). It remains a mystery regarding the relation of calcium and iron ions in PD mechanisms and their contribution to disease susceptibility.

Identifying the cellular causes to neuron death will not only provide more effective disease management but also shed light on molecular signatures shared by a subset of people affected by the disease. A convenient, cost-effective method to spot the vulnerable population, even before the symptom onset, will be extremely valuable for early intervention and preventive medicine. It will improve the efficacy of clinical trials for testing experimental drugs, by facilitating patient stratification and serving as a pharmacodynamic marker.

Understanding disease-causing cellular paths will also help us zoom in on rare genetic variants that contribute to disease etiology but otherwise are difficult to discover through GWAS. Integrating studies of risk variants with disease models and human tissues could establish a causal link of a biological pathway to a disease with complex traits such as PD, with the promise of identifying more effective druggable targets and biomarkers. In this work, we harness the power of combining human genetics, cellular and in vivo models, and patient's tissues, and identify an iron-calcium-Miro axis in PD. Iron accumulation causes mitochondrial calcium overload via promoting MCU oligomerization and its channel activity, which may consequently disturb cellular calcium homeostasis. Miro, a calcium-binding protein, acts downstream of calcium dysregulation. Functional and genetic impairment in this axis may increase PD risk and indicate PD status.

Results

A high-content Miro1 screening assay identifies a network of Ca^{2+}-related drug hits for PD

Miro is an OMM protein essential for mediating mitochondrial motility and safeguarding their quality. Human Miro1 and Miro2 are paralogs with high sequence similarity. We have previously shown that in fibroblasts or neurons derived from sporadic and familial PD patients, Miro1 degradation upon mitochondrial depolarization is delayed, consequently slowing mitophagy and increasing neuronal sensitivity to

stressors (Hsieh et al., 2019; Hsieh et al., 2016; Shaltouki et al., 2018). This Miro1 phenotype would serve as an excellent readout for screening small molecules that promote Miro1 degradation following depolarization. Many compounds in the commonly used screening libraries have well-defined roles and targets, and some show efficacy to treat certain human diseases. This rich information may allow us to reveal cellular pathways underlying the Miro1 phenotype in PD. To this end, we established a sensitive immunocytochemistry (ICC)-based assay that was suitable for high-throughput screening (Figures 1A, S1, S2, S3A, more details in Method). We performed the primary screens at the Stanford High-Throughput Bioscience Center (HTBC) using 3 drug libraries in a sporadic PD fibroblast line. Overall, we identified 35 actives (1.92% primary hit rate) that reduced Miro1 following mitochondrial depolarization (Figures S1, Table S1A-B). To validate the results of the high-content assays, we retested 34 out of the 35 positive Miro1 reducers identified at the Stanford HTBC in our own laboratory using fresh compounds and our confocal microscope. We confirmed that 15 compounds reliably reduced Miro1 protein levels following mitochondrial depolarization in PD fibroblasts (Figure S2, Table S1C). Next, we performed a pathway analysis using a knowledge graph-based tool to reveal the potential cellular pathways connecting Miro1 to each hit compound. Strikingly, we discovered intracellular Ca^{2+} as a primary shared factor in the hit drug-Miro1 network (Figure 1B, Table S2). Two drugs, Benidipine and Tranilast, could directly inhibit plasma membrane Ca^{2+}-channels. Benidipine is a blocker of voltage-gated Ca^{2+}-channels (L-, N-, T-type), and Tranilast has been proposed to inhibit ligand-gated Ca^{2+}-channels (TRPV2) (Darakhshan and Pour, 2015). Dysregulation of Ca^{2+} homeostasis has been widely reported in PD models (Angelova et al., 2020; Apicco et al., 2021; Buttner et al., 2013; Kim et al., 2020; Lee et al., 2018; Surmeier et al., 2017; Tabata et al., 2018; Verma et al., 2017). Our results suggest a direct link of the Ca^{2+}-binding protein, Miro, to Ca^{2+}-mediated abnormality in PD.

Validation of a role for Benidipine in Miro degradation

To understand in detail the relation of Miro with the Ca^{2+}-pathway in Parkinson's pathogenesis, we further examined Benidipine's role in Miro protein stability. Using the same ICC method as in Figure S2, we found that Benidipine reduced Miro1 in a dose-dependent manner in PD fibroblasts treated with carbonyl cyanide 4-(trifluoromethoxy)phenylhydrazone (FCCP) (Figure S3B). To exclude the possibility of any artifacts caused by our ICC method, we verified our results using an entirely different approach to detect Miro1 response to depolarization. We measured Miro1 and additional mitochondrial proteins by Western blotting. We also depolarized mitochondria with a different uncoupler, carbonyl cyanide *m*-chlorophenyl hydrazone (CCCP) (Hsieh et al., 2019), instead of FCCP. We detected Miro1 and mitochondrial markers at 6 and 14 hours after CCCP treatment. We have previously demonstrated that in healthy control fibroblasts following CCCP treatment, Miro1 is degraded earlier (6 hours) than multiple other mitochondrial markers (14 hours) (Figure S3C) (Hsieh et al., 2019; Hsieh et al., 2016), consistent with the observation of proteasomal degradation of Miro1 prior to mitophagy (Chan et al., 2011; Hsieh et al., 2019; Hsieh et al., 2016; Wang et al., 2011). Using this alternative method, we confirmed that both Miro1 degradation and damaged mitochondrial clearance were impaired in the PD cell line we used for screens. Importantly, Benidipine promoted Miro1 degradation after 6 hours following CCCP treatment without affecting the matrix protein ATP5β and facilitated mitochondrial clearance as was evidenced by the degradation of both Miro1 and ATP5β at 14 hours post-treatment (Figure S3C). Interestingly, Miro2 was also resistant to depolarization-induced degradation in PD cells (Hsieh et al., 2019) and Benidipine

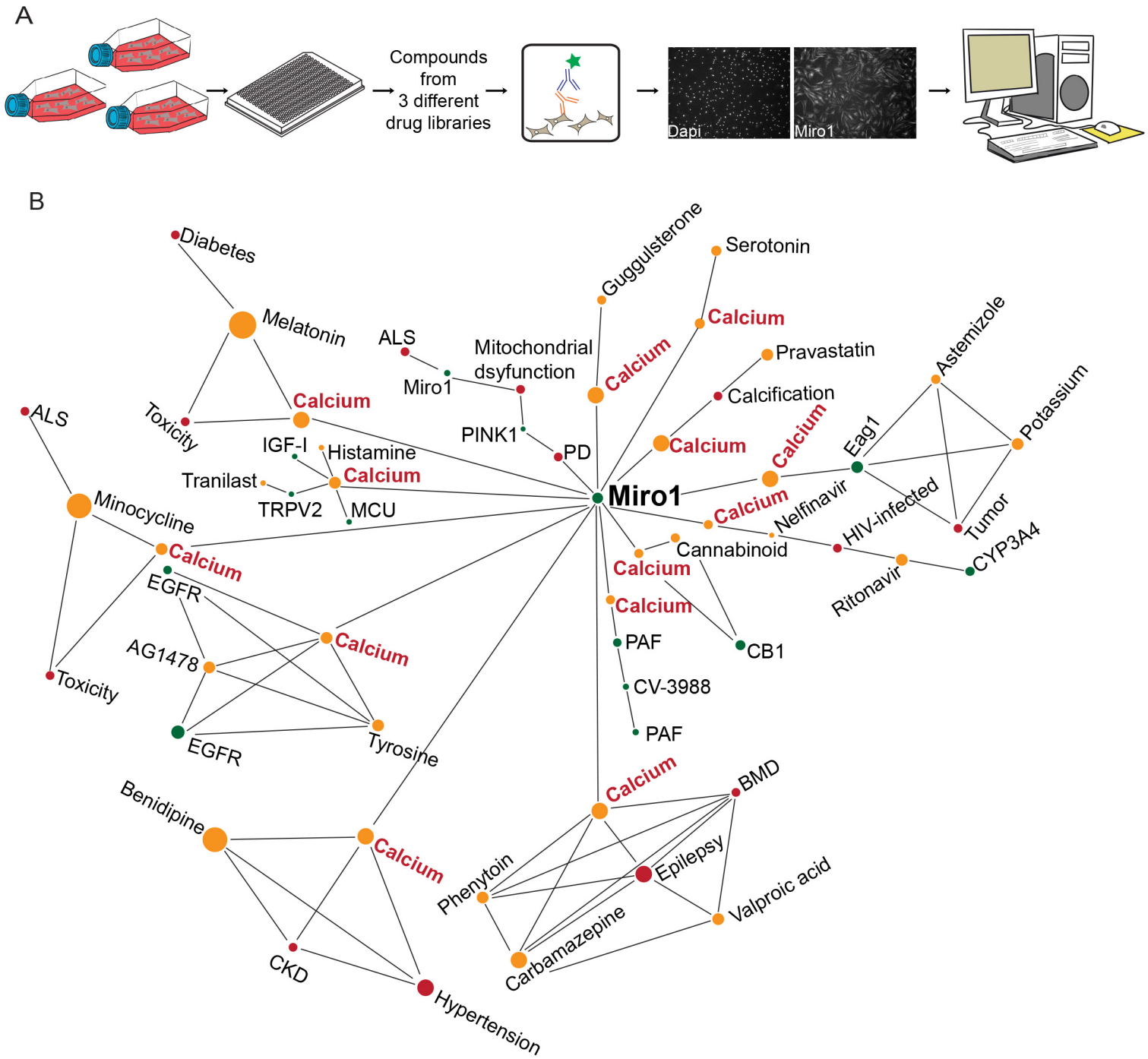

Figure 1. HTP Screens Identify Calcium-Related Drug Hits for PD. (A) Schematic representation of a custom-designed drug screen for Miro1 in PD fibroblasts. (B) Pathway analysis identified calcium as a shared factor in the primary hit-Miro1 network. Each individual pathway is generated using a primary hit and Miro1 as search query and the resulting subnetwork is visualized and curated using docs2graph–a knowledge-graph browser. The visualization shows a subgraph generated by docs2graph from the collection of curated supporting documents for each pathway.

rescued its phenotype (Figure S3C). This result suggests that Miro1 and Miro2, which share the Ca^{2+}-binding EF-hands, are functionally redundant in the Ca^{2+}-dependent regulation. We confirmed that Benidipine did not affect *Miro1* messenger RNA (mRNA) expression detected by reverse transcription quantitative real-time PCR (RT-qPCR) under basal and depolarized conditions in PD cells (Figure S3D). Neither did Benidipine alter the basal ATP levels (Figure S3E), nor the mitochondrial membrane potential measured by TMRM staining (Figure S3F). Collectively, we have demonstrated that Benidipine, a Ca^{2+}-channel blocker, specifically promotes Miro degradation upon depolarization in PD fibroblasts using multiple methods.

Benidipine rescues Parkinson's phenotypes in human neuron and fly models of PD

We have previously shown that reducing Miro rescues Parkinson's phenotypes in cellular and in vivo models (Hsieh et al., 2019; Hsieh et al., 2016; Li et al., 2021; Shaltouki et al., 2018), suggesting that small molecules that lower Miro protein levels could represent an effective therapeutic approach for PD. From our high-throughput screens we have discovered that Benidipine, which targets the Ca^{2+} pathway, promotes Miro degradation upon depolarization in skin cells of a PD patient (Figures 1, S1-3). We next tested whether Benidipine was useful for alleviating Parkinson's phenotypes in two independent models: the human neuron and fly models. We examined Benidipine using induced pluripotent stem cells (iPSCs) from one familial patient with the A53T mutation in *SNCA* (encodes α-synuclein) and its isogenic wild-type control (Hsieh et al., 2019; Hsieh et al., 2016; Li et al., 2021; Shaltouki et al., 2018). We differentiated iPSCs to neurons expressing tyrosine hydroxylase (TH), the rate-limiting enzyme for DA synthesis as previously described (Figure S4A) (Hsieh et al., 2019; Hsieh et al., 2016; Li et al., 2021; Shaltouki et al., 2018). These patient-derived neurons display increased expression of endogenous α-synuclein (Shaltouki et al., 2018). We identified DA neurons by TH-immunostaining and cell death by terminal deoxynucleotidyl transferase dUTP nick end labeling (TUNEL)-staining (Li et al., 2021; Shaltouki et al., 2018) (Figures 2A-B, S4A). We have previously shown that iPSC-derived DA neurons from PD patients are more vulnerable to stressors than those from healthy controls (Hsieh et al., 2019; Hsieh et al., 2016; Li et al., 2021; Shaltouki et al., 2018). The treatment of the complex III inhibitor, Antimycin A, at 10 μM for 6 hours caused acute neuronal cell death leading to the loss of TH and the increase of TUNEL signals in neurons derived from the PD patient (Hsieh et al., 2019; Li et al., 2021; Shaltouki et al., 2018) (Figure 2A-B). Notably, Benidipine treatment at 10 μM for 30 hours significantly rescued this stressor-induced neuron death (Figure 2A-B).

In order to cross-validate the neuroprotective effect of Benidipine in vivo, we fed Benidipine to a fly model of PD, which expressed the pathogenic human α-synuclein protein with the A53T mutation (α-syn-A53T) in DA neurons driven by *TH-GAL4* (Hsieh et al., 2019; Li et al., 2021; Shaltouki et al., 2018). These flies exhibit PD-relevant phenotypes such as age-dependent locomotor decline and DA neuron loss (Hsieh et al., 2019; Li et al., 2021; Shaltouki et al., 2018). Importantly, feeding PD flies with 2.5 μM Benidipine from adulthood prevented DA neuron loss in aged flies (Figure 2C) and improved their locomotor ability (Figure 2D). Taken together, Benidipine, which eliminates the Miro1 defect in PD fibroblasts, rescues PD-related phenotypes in human neuron and fly models.

The EF-hands of Miro play a role in causing Parkinson's-relevant phenotypes

Having demonstrated a link between Miro and Ca^{2+} in multiple models of PD, we next determined whether Ca^{2+} directly interacted with Miro to contribute to phenotypes in these models. To achieve this goal, we made GFP-tagged human Miro1 protein in both the wild-type (Miro1-WT) form and in a mutant form where

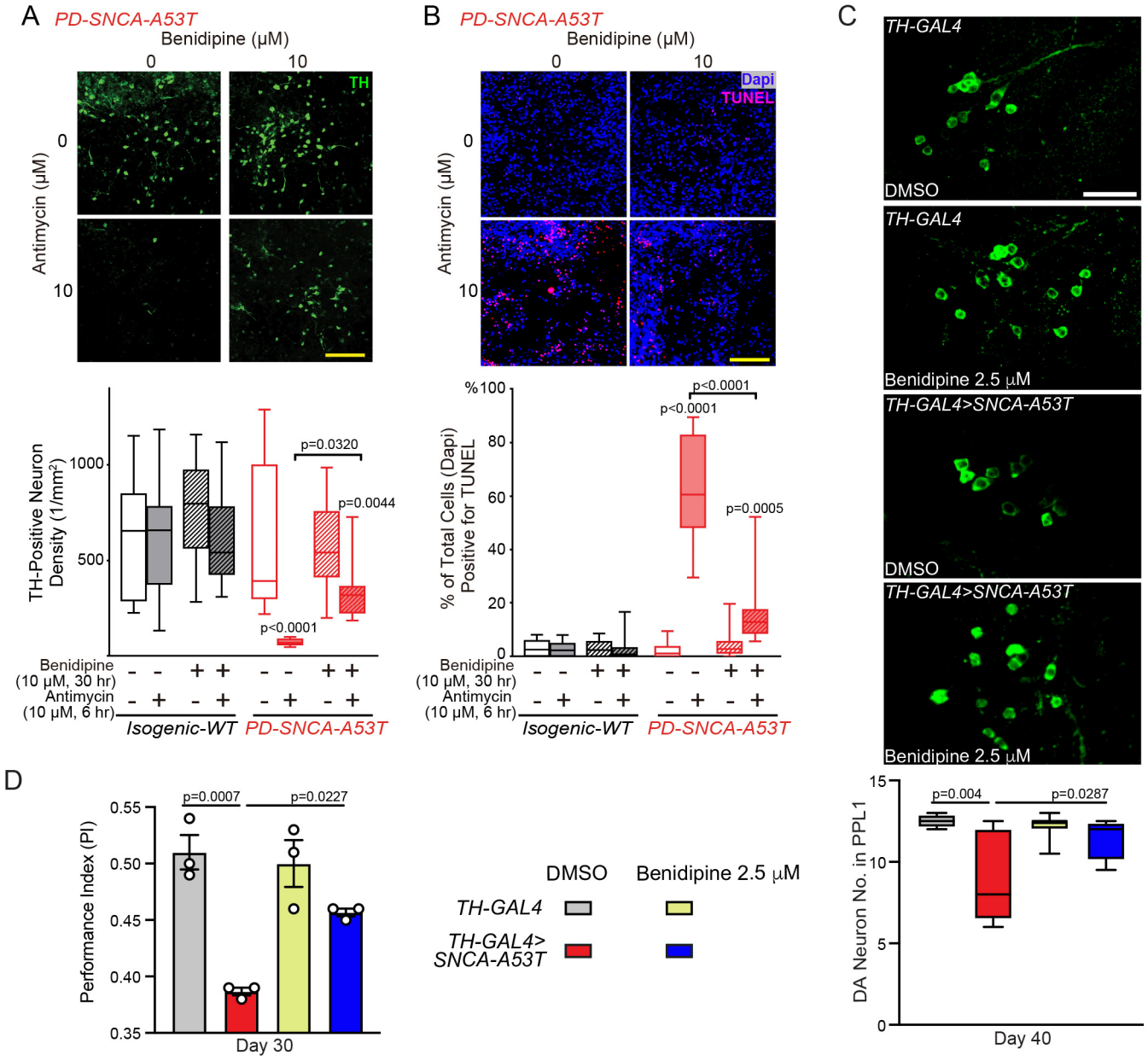

Figure 2. Benidipine Rescues PD Relevant Phenotypes. (A-B) iPSC-derived neurons from a PD patient with SNCA-A53T and the isogenic control, treated as indicated, were immunostained with anti-TH (A) or TUNEL and Dapi (B), and imaged under a confocal microscope. Scale bars: 100 um. Below: Quantifications of the density of TH-positive neurons (A) or the percentage of TUNEL-positive neurons (B). n=20 images from 3 independent coverslips. P values are compared with the far-left bar, except indicated otherwise. (C) 40-day-old fly brains were immunostained with anti-TH and the DA neuron number was counted in the PPL1 cluster. Scale bar: 20 um. n=4, 7, 7, 4 (from left to right). (D) The Performance Index was measured in 30-day-old flies, fed as indicated. n=59, 57, 54, 57 flies (from left to right), 3 independent experiments. (C-D) Drug treatment was started from adulthood (day 1). One-Way Anova Post Hoc Tukey Test for all panels.

two point mutations were introduced in the two EF-hands of Miro1 (Miro1-KK) to block Ca^{2+}-binding (Wang and Schwarz, 2009). We expressed GFP-tagged Miro1 (WT or KK) and Mito-dsRed that labeled mitochondria in iPSC-derived neurons from the PD patient and isogenic control, described earlier. We chose the distal segment of the axon for analysis (Hsieh et al., 2016). We have previously shown that following 100 μM Antimycin A treatment that triggers mitophagy, Miro1 and mitochondria are sequentially degraded in wild-type neurons (Hsieh et al., 2019; Hsieh et al., 2016; Shaltouki et al., 2018). We observed the same mitochondrial events in isogenic control axons transfected with GFP-Miro1-WT. Within 25 min GFP-Miro1-WT was partially degraded, and within 58 min mitochondrial clearance was induced (Figure 3A-C). In contrast, in PD neuron axons transfected with GFP-Miro1-WT, the degradation rates of both Miro1 and damaged mitochondria upon Antimycin A treatment were slowed (Figure 3A-C), consistent with our previous studies (Hsieh et al., 2019; Shaltouki et al., 2018). Notably, GFP-Miro1-KK significantly rescued these phenotypes in PD axons: it expedited the degradation rates to the control level (Figure 3A-C). These data suggest that Miro1 directly binds to Ca^{2+} to mediate mitochondrial phenotypes in PD neurons, at least in part.

To confirm the Miro-Ca^{2+} relation in vivo, we generated transgenic flies carrying T7-tagged fly Miro (DMiro)-WT or DMiro-KK. DMiro is an ortholog of human Miro1 and Miro2. Both DMiro-WT and DMiro-KK were expressed at comparable levels when the transgenes were driven by the ubiquitous driver *Actin-GAL4* (Figure S4B). We next crossed these transgenic flies to a fly PD model described earlier that expressed human α-syn-A53T in DA neurons driven by *TH-GAL4*. Consistent with the results from human neurons, DMiro-KK significantly rescued the PD-relevant phenotypes including the age-dependent DA neuron loss and locomotor decline, as compared to DMiro-WT (Figure 3D-E). Altogether, we have provided evidence showing that the Ca^{2+}-binding domain of Miro plays a key role in causing phenotypes in human neuron and fly models of PD.

Mitochondria accumulate Ca^{2+}, Fe^{2+}, and reactive oxygen species in PD neurons

Our results, showing that either blocking Ca^{2+}-entry into the cell or inhibiting Ca^{2+}-binding to Miro rescues the Miro and neurodegenerative phenotypes in PD models (Figures 1-3), placed Ca^{2+} dysregulation upstream of Miro. We next dissected how Ca^{2+}-handling was mis-regulated in neurons derived from the PD patient (Figures 2-3). We stimulated these neurons with the G-protein-coupled receptor (GPCR) agonist, thrombin, and measured cytosolic and mitochondrial Ca^{2+} levels with live Calcium Green and Rhod-2 staining, respectively. We found that thrombin triggered intracellular Ca^{2+} mobilization and elevation, which was comparable between PD and isogenic control neurons (Figure 4A). However, mitochondria in PD neurons sustained significantly larger Ca^{2+}-elevation after thrombin stimulation, as compared to control (Figure 4A). These results indicate that the mitochondrial Ca^{2+}-uptake ability is enhanced in PD neurons.

Iron accumulation and oxidative stress are also hallmarks of PD (Belaidi and Bush, 2016). We next examined mitochondrial Fe^{2+} and reactive oxygen species (ROS) levels in these PD neurons. We discovered a significant increase in both the mitochondrial Fe^{2+} detected by RPA (Figure 4B) and ROS levels detected by MitoNeoD (Shchepinova et al., 2017) staining (Figure 4C), in PD neurons compared to isogenic control. Hence, Ca^{2+}, Fe^{2+}, and ROS are all accumulated in PD mitochondria.

Iron promotes the assembly of MCU oligomers

The enhanced mitochondrial Ca^{2+}-uptake observed in PD neurons (Figure 4A) led us to investigate the Ca^{2+}-uptake channel in the IMM–MCU. Because MCU oligomerization is

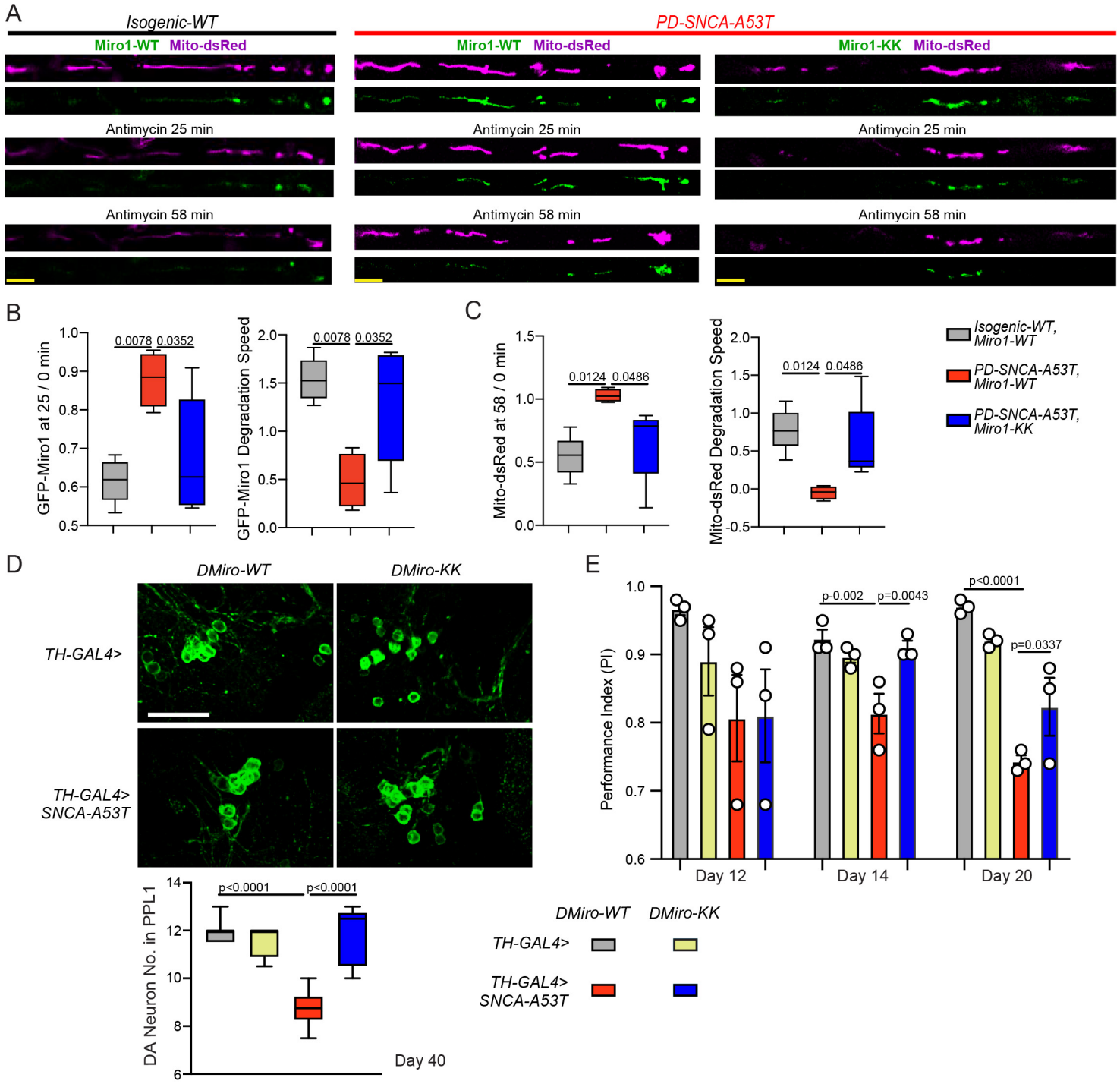

Figure 3. The EF-hands of Miro Play a Role in Causing PD Relevant Phenotypes. (A) Representative still images from live Mito-dsRed and GFP-Miro1 imaging movies of axons of indicated genotypes, following 100 uM Antimycin A treatment. Scale bar: 10 um. (B) Left: Quantification of the GFP-Miro1 intensity at 25 minutes divided by that at 0 minute following 100 uM Antimycin A treatment from the same axonal region. Right: Quantification of the reduction speed of the GFP-Miro1 intensity within 25 minutes following 100 uM Antimycin A treatment. (C) Left: Quantification of the Mito-dsRed intensity at 58 minutes divided by that at 0 minute following 100 uM Antimycin A treatment from the same axonal region. Right: Quantification of the Mito-dsRed intensity reduction speed within 58 minutes following 100 uM Antimycin A treatment. (B-C) n=5, 4, 5 (from left to right) axons (one axon per coverslip). (D) The DA neuron number was counted in the PPL1 cluster of flies with indicated genotypes. Scale bar: 20 um. n=7, 4, 6, 5 (from left to right). (E) The Performance Index was measured in flies with indicated genotypes and age. n (from left to right)=49, 47, 40, 47 flies (day 12); 49, 47, 39, 47 (day 14); 48, 45, 37, 44 (day 20); 3 independent experiments. One-Way Anova Post Hoc Tukey Test for all panels.

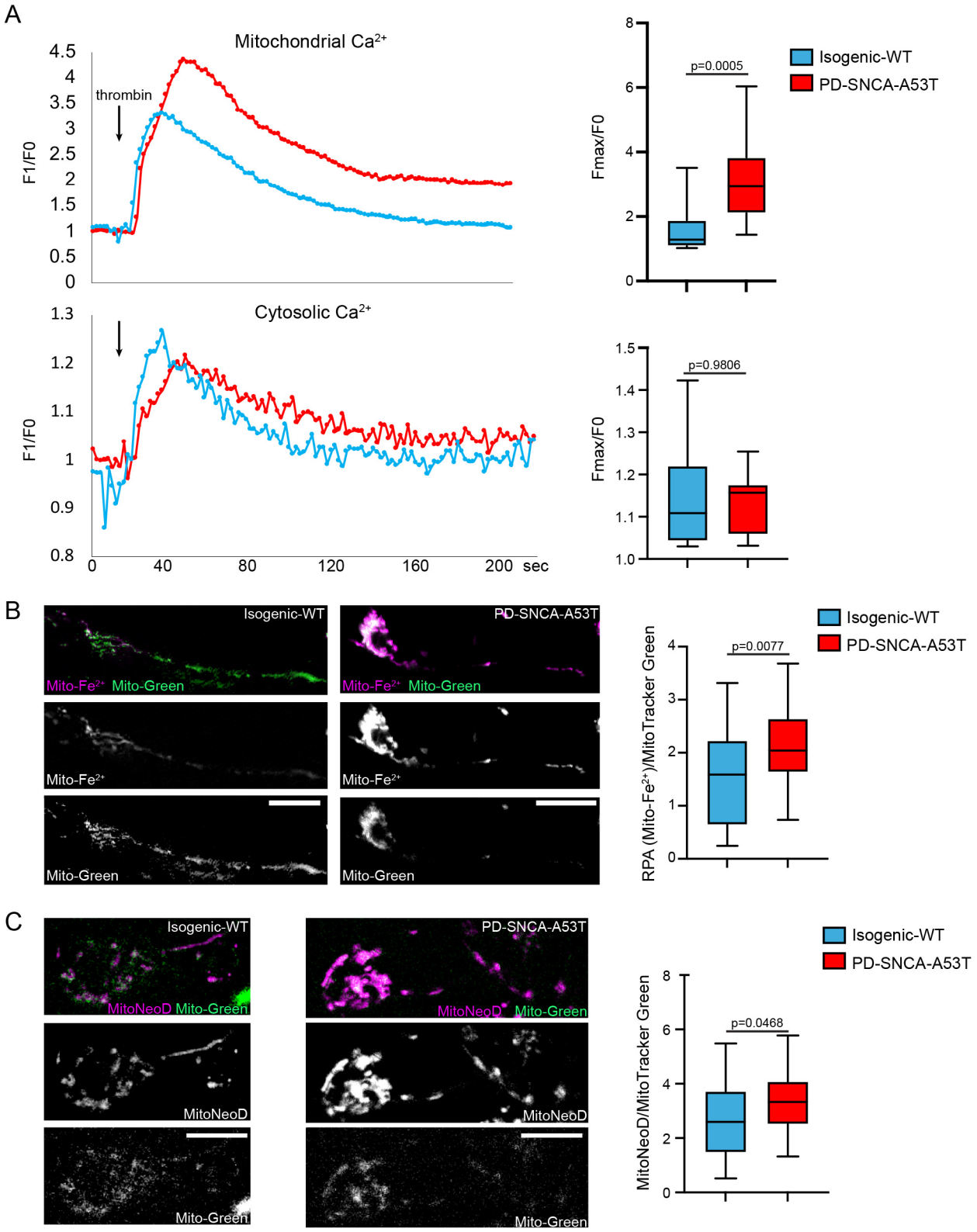

Figure 4. PD Mitochondria Accumulate Ca2+, Fe2+, and ROS. (A) iPSC-derived neurons from a PD patient with SNCA-A53T and the isogenic control were stimulated with thrombin and mitochondrial (Rhod-2) and cytosolic Ca2+ levels (Calcium Green) were measured. Left: Representative traces of Ca2+ ions in neurons. Right: Quantifications of the peak fluorescent intensity normalized to baseline. n=15 cell bodies from 3 independent coverslips. (B) Left: Confocal single section images of live neurons as in (A) stained with RPA (mitochondrial Fe2+–Mito-Fe2+) and MitoTracker Green (Mito-Green). Right: Quantifications of the RPA fluorescent intensity normalized to MitoTracker Green. n=26 (WT) and 28 (PD) cell bodies from 3 coverslips. (C) Left: Confocal single section images of live neurons stained with MitoNeoD and MitoTracker Green (Mito-Green). Right: Quantifications of the MitoNeoD fluorescent intensity normalized to MitoTracker Green. n=25 cell bodies from 3 coverslips. Two-tailed Welch's T Test for all panels. Scale bars: 10 um.

essential for MCU's function to import Ca^{2+} into the mitochondria (Dong et al., 2017; Fan et al., 2018; Fan et al., 2020), we explored the possibility that MCU oligomerization was affected by Fe^{2+}, Ca^{2+}, or ROS, small molecules elevated in PD neuronal mitochondria (Figure 4). We performed size exclusion chromatography (SEC), where protein complexes with higher molecular weight (MW) are eluted faster than those with lower MW, using lysates of HEK cells treated by Fe^{2+}, Ca^{2+}, or H_2O_2. Detecting MCU from cell lysates using SEC has been successfully shown (Dong et al., 2017; Lambert et al., 2019; Tomar et al., 2016). We found that Fe^{2+}, Ca^{2+}, and H_2O_2 treatment all shifted the MCU elution peaks to the earlier fractions with higher-order oligomers than control (Figure 5A-E; anti-MCU was validated in Figure S4C). In contrast, the elution pattern of Miro1 was largely unaltered by any of these treatments, except that Ca^{2+} treatment slightly shifted the peak to the later fraction (Figure 5A-D). These results show that intracellular small molecules including iron, Ca^{2+}, and H_2O_2 (Dong et al., 2017) can influence the equilibrium of MCU oligomeric complexes and may consequently alter the MCU channel activity.

SEC is a sensitive method to detect protein composition dynamics, while Native-PAGE can determine the overall form and amount of a multimeric native protein. The human MCU oligomer bands from HEK cells migrated between 400-700 KDa in Native-PAGE (Figure 5F; the negative control in the left lane, *MCU-/-,* showed no signal) (Baughman et al., 2011; Ghosh et al., 2020; Tomar et al., 2016). Importantly, we found that Fe^{2+} treatment, but not Ca^{2+} or H_2O_2, resulted in an increase in the total intensity of the MCU oligomer bands (Figure 5F). Miro1 protein also oligomerized and migrated as a single band around 480 KDa in Native-PAGE, which was not significantly affected by any of these treatments (Figure 5F). These data indicate that iron not only shifts the MCU complexes to higher-order oligomers but also enlarges the total number of these complexes, and thus may have a more profound impact on the MCU activity than Ca^{2+} and H_2O_2.

We next examined the levels of additional mitochondrial membrane proteins that may assist the MCU function using HEK cells. When Fe^{2+} was added in media and lysis buffer, we found that MCUb and NCLX were lowered, but not any other proteins examined (Figure S5). MCUb is an inhibitor of MCU (Lambert et al., 2019), and NCLX is an IMM exchanger believed for mitochondrial Ca^{2}-extrusion (Lee et al., 2016; Palty et al., 2010). The reduction of both proteins could exacerbate the phenotype of mitochondrial Ca^{2+}-overload. Taken together, our results show that iron promotes MCU oligomerization and may cause Ca^{2+}-accumulation inside the mitochondria.

Fe^{2+} binds to the MCU complex and acts on its Ca^{2+}-import ability

We probed the mechanism underlying the observed impact of iron on MCU oligomerization (Figure 5). One hypothesis was that the MCU complex bound to iron leading to conformational changes. To explore this possibility, we immunoprecipitated (IP) endogenous MCU from HEK cells and detected the iron concentrations in the IP samples. We found significantly more Fe^{2+} ions pulled down with MCU when HEK cells were treated with Fe^{2+}, compared with other controls (Figure 6A). This result shows that the MCU complex interacts with Fe^{2+}. To determine whether MCU directly bound to Fe^{2+}, we switched our experiments to an in vitro setting. To circumvent the problem of precipitation caused by a fast speed of Fe^{2+} oxidation in vitro, we used an Fe^{2+} mimic, Co^{2+} ion (Billesbolle et al., 2020). We first confirmed that Co^{2+} behaved similarly as Fe^{2+} in our functional assays in HEK cells: Co^{2+} treatment increased MCU oligomerization detected by Native-PAGE (Figure 6B), just like Fe^{2+} (Figures 5F, 6B), and both Fe^{2+} and Co^{2+} treatment enhanced the mitochondrial Ca^{2+}-uptake ability following thrombin application (Figure 6C). Using fluorescence-detection SEC

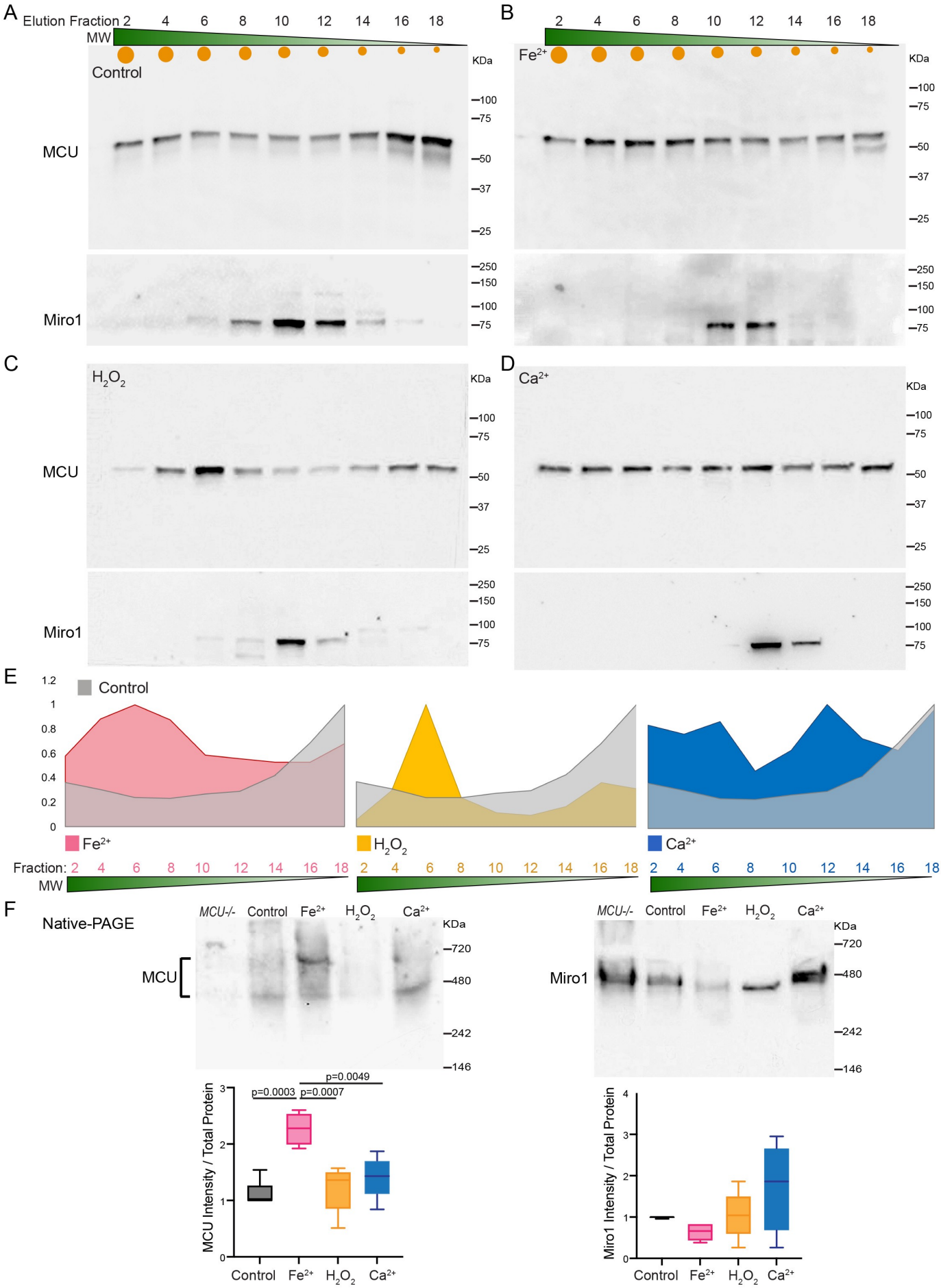

Figure 5: Iron Promotes MCU Oligomerization. (A-D) HEK cells were treated as indicated and run through SEC. Fractions were run in SDS-PAGE and blotted. (E) Elution profiles for (A-D). (F) HEK cells were treated similarly as above, run in Native-PAGE, and blotted. Below: Qualifications of the band intensities normalized to the total protein amount measured by BCA. n=5 independent experiments. One-Way Anova Post Hoc Tukey Test.

on purified human MCU protein (Fan et al., 2020), we found that Co^{2+} caused the formation of higher-order oligomers of MCU, and decreased MCU protein stability with increased temperature (Figure 6D-E). These results demonstrate that the Fe^{2+} mimic, Co^{2+}, directly binds to MCU, increasing its oligomerization.

We next searched for amino acid residues in the matrix domain of MCU (PDB: 5KUE) predicted to bind to Fe^{2+} using an in-silico program (http://bioinfo.cmu.edu.tw/MIB/) (Lin et al., 2016; Lu et al., 2012), and found 3 amino acids: 74D, 148D, and 159H. The latter 2 residues were also predicted to bind to Co^{2+}. We mutated these 3 sites to Alanine (named "MCU-3A"). To determine whether these mutations were sufficient to eliminate the Fe^{2+}-triggered oligomerization of MCU, we expressed Flag-tagged MCU-WT or MCU-3A in HEK cells without endogenous MCU (*MCU-/-*), treated these cells with Fe^{2+}, and ran the lysates in Native-PAGE. Indeed, MCU-3A completely abolished MCU's response to Fe^{2+} treatment: the MCU oligomer band intensity was no longer increased (Figure 6F). We then live imaged mitochondrial Ca^{2+}-dynamics, as described in Figure 4A, in these cells. We consistently observed a larger mitochondrial Ca^{2+}-elevation following thrombin stimulation in MCU-WT-transfected HEK cells treated with Fe^{2+} as compared to no Fe^{2+}-treatment, and MCU-3A blunted the peak increase (Figure 6G-H). Because Fe^{2+} also lowered NCLX levels (Figure S5) which could affect mitochondrial Ca^{2+}-extrusion, we measured the mitochondrial Ca^{2+}-efflux rate. Indeed, Fe^{2+} treatment slowed the efflux rate, which was prevented by MCU-3A (Figure 6I), suggesting that the Fe^{2+}-triggered efflux delay might depend on Ca^{2+}-overload. Altogether, our results show that Fe^{2+} binds to the MCU complex, promoting MCU oligomerization and its channel activity.

Iron functions upstream of calcium to mediate phenotypes of PD neurons

Our discovery of the action of Fe^{2+} on the MCU activity (Figures 5-6) suggested that in PD neurons, the elevation of mitochondrial Fe^{2+}-levels (Figure 4B) could be one of the main reasons for mitochondrial Ca^{2+}-overload (Figure 4A). To confirm their causal relation, we treated PD neurons with deferiprone (DFP), an iron chelator (Munson et al., 2021). Indeed, DFP significantly reduced mitochondrial Ca^{2+}-accumulation following thrombin stimulation (Figure 7A) and prevented cell death triggered by Antimycin A treatment (Figure 7B) in iPSC-derived neurons from the familial PD patient described earlier. We treated neurons from a second, sporadic patient with DFP and saw a similar neuroprotective effect (Figure 7B). In vivo, feeding the fly model of PD as shown earlier (Figures 2-3) with DFP consistently rescued the PD-relevant phenotypes, including age-dependent DA neuron loss and locomotor decline (Figure 7C-D). Collectively, our results show that iron functions upstream of calcium to mediate neurodegeneration in PD models.

MCU, MCUb, and NCLX are affected in PD postmortem brain

Our finding showing that iron impacts mitochondrial Ca^{2+}-channels and transporters (Figure 5F, 6B, S5) prompted us to examine these proteins in postmortem brains of people with PD, diffuse Lewy body disease (DLBD), or Alzheimer's disease (AD) (Table S3). We homogenized the frontal cortex and ran the brain lysate in Native- or SDS-PAGE. We focused on MCU oligomers, NCLX, and MCUb, which were shown earlier specifically altered by Fe^{2+} treatment in HEK cells (Figure 5F, 6B, S5). We found the PD group clustered and separated from the healthy control group, with higher intensity of the MCU oligomer bands and lower intensity of both the NCLX and MCUb bands (Figure 7E), similar to the observations in HEK cells treated with Fe^{2+} (Figure 5F, 6B, S5). This unique clustering was not observed in the AD or DLBD group (Figure 7E, S6). Together, our data suggest that the combined functional impairment of

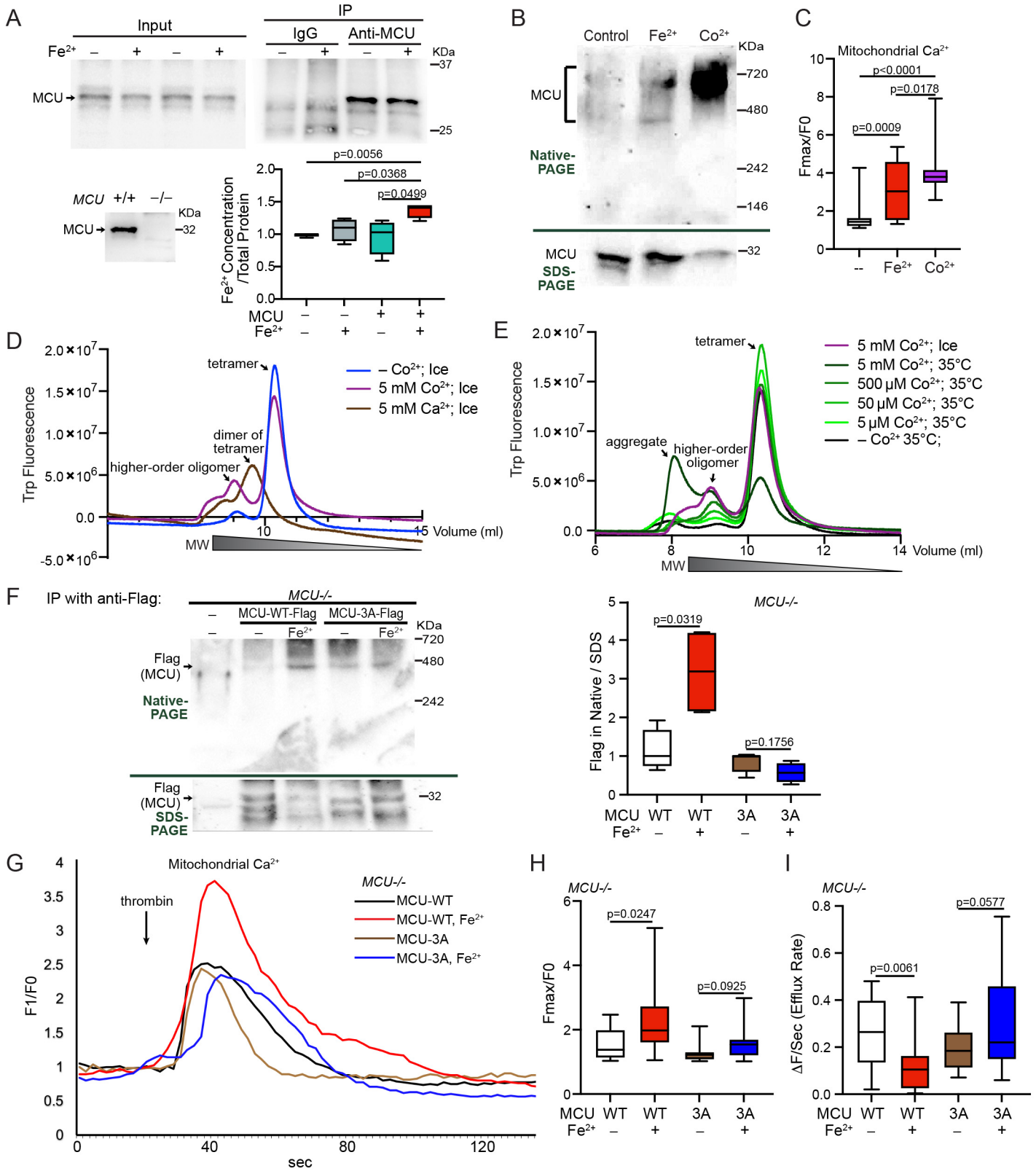

Figure 6. MCU Binds to Fe2+. (A) HEK cells were treated with or without 5 mM Fe2+ for 21 hours, then IPed with rabbit IgG or anti-MCU, and Fe2+ concentrations in the IP samples were detected. n=4 independent experiments. Top western blots demonstrated the success of IP. Anti-MCU was validated using MCU-/- HEK cell lysate (bottom panel). Arrow indicates the MCU band. (B) HEK cells were treated with 5 mM Fe2+ or Co2+ for 22 hours and lysed in buffer containing the same metal. Lysates were run in Native- or SDS-PAGE and blotted with anti-MCU. Similar results were seen for at least 3 times. (C) HEK cells treated with 5 mM Fe2+ or 500 uM Co2+ for 22 hours were stimulated with thrombin and mitochondrial Ca2+ levels (Rhod-2) were measured. The peak fluorescent intensity normalized to baseline is quantified. n=20 cells from 4 independent coverslips. (D-E) Fluorescence-detection SEC profiles of purified human MCU. The annotation of the peaks is based on (Fan et al., 2018; Fan et al., 2020). (F) Left: Representative blots of IP with anti-Flag using cell lysates as indicated, run in Native- or SDS-PAGE. Right: Quantification of the band intensity of MCU-Flag in Native-PAGE normalized to that in SDS-PAGE from the same experiment. n=4 independent experiments. (G) HEK cells treated as indicated were stimulated with thrombin and mitochondrial Ca2+ levels (Rhod-2) were measured. Representative traces of Ca2+ ions. (H-I) Based on traces like in (G), the peak fluorescent intensity normalized to baseline (H) or efflux rate (I) is quantified. n=17 cells from 4 independent coverslips. Two-tailed Welch's T Test for all panels.

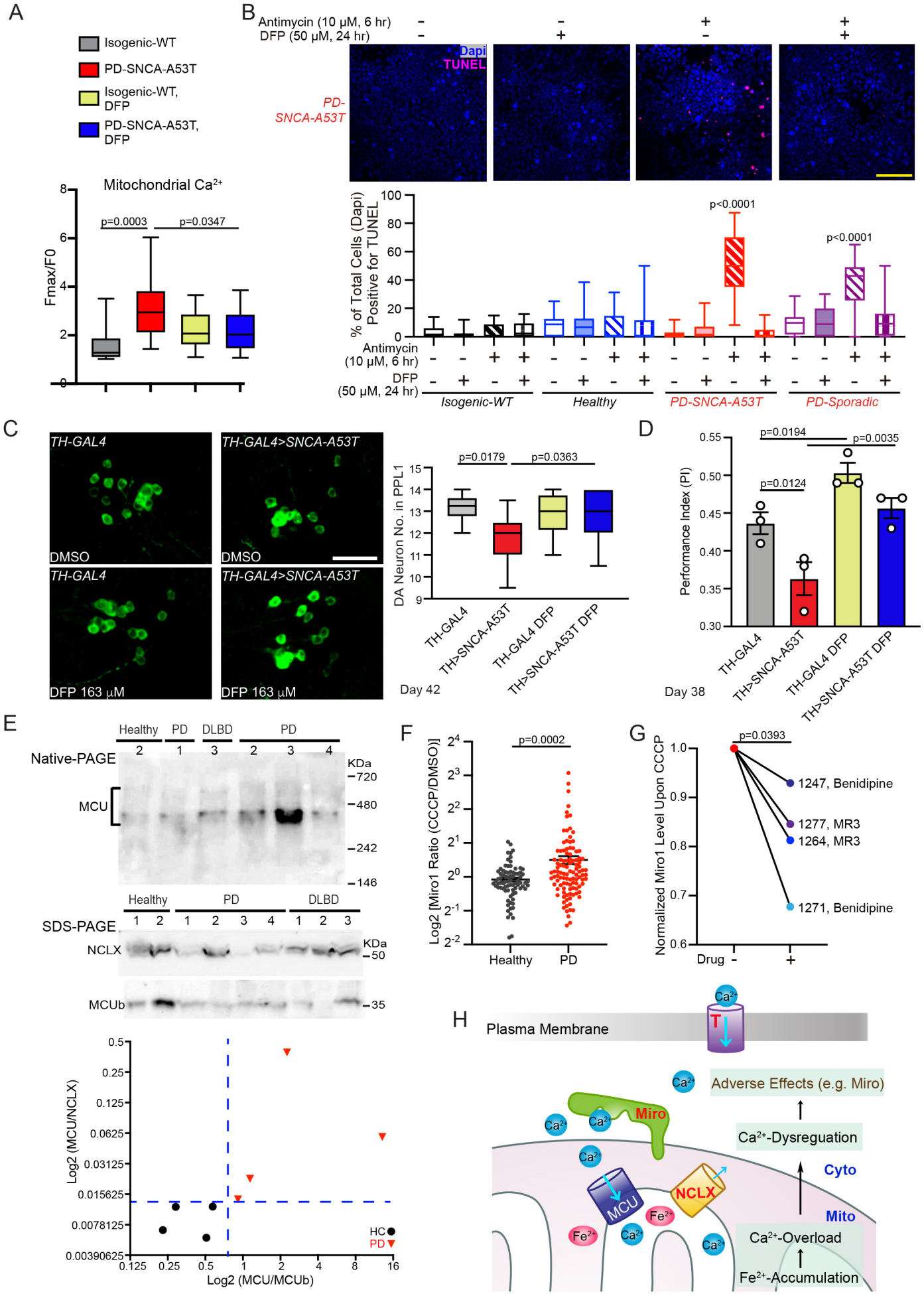
A
Isogenic-WT
PD-SNCA-A53T
Isogenic-WT, DFP
PD-SNCA-A53T, DFP
Mitochondrial Ca2+
Fmax/F0
p=0.0003
p=0.0347
B
Antimycin (10 μM, 6 hr)
DFP (50 μM, 24 hr)
Dapi
TUNEL
PD-SNCA-A53T
% of Total Cells (Dapi) Positive for TUNEL
p<0.0001
p<0.0001
Antimycin (10 μM, 6 hr)
DFP (50 μM, 24 hr)
Isogenic-WT
Healthy
PD-SNCA-A53T
PD-Sporadic
C
TH-GAL4
TH-GAL4>SNCA-A53T
DMSO
DFP 163 μM
DA Neuron No. in PPL1
p=0.0179
p=0.0363
TH-GAL4
TH>SNCA-A53T
TH-GAL4 DFP
TH>SNCA-A53T DFP
Day 42
D
Performance Index (PI)
p=0.0194
p=0.0035
p=0.0124
Day 38
E
Healthy
PD
DLBD
Native-PAGE
MCU
KDa
720
480
242
146
SDS-PAGE
NCLX
MCUb
50
35
Log2 (MCU/NCLX)
Log2 (MCU/MCUb)
HC
PD
F
Log2 [Miro1 Ratio (CCCP/DMSO)]
p=0.0002
Healthy
PD
G
Normalized Miro1 Level Upon CCCP
p=0.0393
1247, Benidipine
1277, MR3
1264, MR3
1271, Benidipine
Drug
H
Plasma Membrane
Adverse Effects (e.g. Miro)
Miro
Ca2+-Dysregulation
Cyto
MCU
NCLX
Mito
Ca2+-Overload
Fe2+-Accumulation

Figure 7. Chelating Iron Restores Ca2+ and neuronal homeostasis in PD neurons. (A) Similar to Figure 4A, iPSC-derived neurons from a PD patient with SNCA-A53T and the isogenic control, with or without treatment of 100 uM DFP for 24 hours, were stimulated with thrombin, and mitochondrial Ca2+ (Rhod-2) was measured. Quantifications of the peak fluorescent intensity normalized to baseline. n=15 cell bodies from 3 independent coverslips. Control data without DFP treatment are the same as in Figure 4A. One-Way Anova Post Hoc Tukey Test. (B) iPSC-derived neurons treated as indicated, were immunostained with TUNEL and Dapi, and imaged under a confocal microscope. Scale bar: 50 um. Below: Quantification of the percentage of TUNEL-positive neurons. n=20 images from 3 independent coverslips. P values are compared within each genotype (significant compared to every other condition) with One-Way Anova Post Hoc Tukey Test. (C) The DA neuron number was counted in the PPL1 cluster of flies with indicated genotypes and conditions. Drug treatment was started from adulthood (day 1). Scale bar: 20 um. n=6, 9, 8, 7 (from left to right). (D) The Performance Index was measured in flies. Drug treatment was started from embryogenesis. n=35, 33, 40, 34 flies (from left to right), 3 independent experiments. (C-D) One-Way Anova Post Hoc Tukey Test. (E) Postmortem brains were run in Native- or SDS-PAGE and blotted. The band intensity normalized to the total protein level measured by BCA is divided by that of the universal control on the same blot: CVD (cardiovascular disease), which was included on every blot. The MCU oligomer bands in Native-PAGE and the NCLX and MCUb bands in SDS-PAGE (average of 3 replicates) are used in the plot. HC: healthy control. (F) Miro1 protein levels were measured using ELISA in PBMCs treated with DMSO or 40 uM CCCP for 6 hours. Miro1 Ratio is calculated by dividing the Miro1 value treated with CCCP by that with DMSO from the same subject. Dot plot with Mean±S.E.M. n=80 healthy controls and 107 PD. Two-tailed Welch's T Test. (G) PBMCs from 4 PD patients were treated with 40 uM CCCP for 6 hours, or pretreated with 10 uM Benidipine or MR3 for 18 hours and then with 40 uM CCCP for another 6 hours, and Miro1 protein was detected using ELISA. Patient IDs are the same as in Table S4. Two-tailed paired T Test. (H) Schematic representation of the iron-calcium-Miro axis discovered in this study. Red texts show genes containing variants associated with PD.

MCU, MCUb, and NCLX may be one of the molecular signatures shared by people with PD.

Miro1 in blood cells reflects PD status and responds to drug treatment

Now we have demonstrated a functional axis of iron-calcium-Miro in neurons of our PD models and patients. We next sought evidence of its impairment in peripheral tissues of PD patients, which could serve as an excellent candidate for biomarker and pharmacodynamic marker development. Measuring the combined impairment of MCU oligomerization, MCUb, and NCLX requires a large amount of protein and Native-PAGE, which is not applicable for high-throughput screening and clinical practice. We then explored Miro1, whose slower degradation following mitochondrial depolarization was downstream of Ca^{2+}-dysregulation in our PD models, as shown earlier (Figures 1-3). Notably, we have previously found that in skin fibroblasts and iPSCs the delay of Miro1 degradation upon depolarization distinguishes PD patients and genetic carriers from healthy controls (Hsieh et al., 2019; Hsieh et al., 2016; Nguyen et al., 2021). Although fibroblasts can be readily obtained by a skin biopsy, a blood test remains the most convenient method. We investigated whether Miro1 could be detected in peripheral blood mononuclear cells (PBMCs) acquired from a blood draw. We cultured PBMCs from a healthy donor from the Stanford Blood Center (SBC, Table S4) and depolarized the mitochondrial membrane potential using two different methods: Antimycin A plus Oligomycin (Ordureau et al., 2020), or CCCP. We found that both methods caused the degradation of Miro1 and additional mitochondrial markers in a time-dependent manner, detected by Western blotting (Figure S7A-B), consistent with other cell types (Hsieh et al., 2019; Hsieh et al., 2016; Nguyen et al., 2021).

To enable high-content screening, we applied an enzyme-linked immunosorbent assay (ELISA) of Miro1 (Figure S7C-D) to PBMCs from the same donor with 6-hour CCCP treatment. We saw a similar Miro1 response to CCCP using ELISA (SBC, Table S4). We then used this ELISA to screen a total of 80 healthy controls and 107 PD patients (Table S4). Miro1 Ratio (Miro1 protein value with CCCP divided by that with DMSO from the same person) was significantly higher in PD patients compared to healthy controls (Figure 7F, Table S4), indicating that Miro1 is more stable upon depolarization in PD patients.

To determine whether our method could be used to classify an individual into a PD or healthy group, we employed machine learning approaches using our dataset. We trained a logistic regression model to assess the impact of Miro1 Ratio on PD, solely on its own or combined with additional demographic and clinical parameters (Method). Unified Parkinson's Disease Rating Scale (UPDRS) is a tool to measure motor and non-motor symptoms of PD which may reflect disease severity and progression. Using UPDRS, our model yielded an accuracy (an individual was correctly classified as with PD or healthy) of 81.2% ($p<0.000001$; area under the Receiver Operator Curve (ROC)–AUC=0.822), and using Miro1 Ratio, the accuracy was 67.6% ($p=0.03$; AUC=0.677). Notably, if both Miro1 Ratio and UPDRS were considered, our model generated an improved accuracy of 87.8% ($p=0.02$; AUC=0.878), without the interference of age or sex (Method, Figure S7E-F). Therefore, our results suggest that the molecular (Miro1 Ratio) and symptomatic (UPDRS) evaluations may reveal independent information, and that combining both tests may more accurately categorize individuals with PD and measure their responses to experimental therapies.

To probe the potential utilization of this Miro1 assay in future clinical trials for stratifying patients or monitoring drug efficacy, we treated PBMCs from 4 PD patients (Table S4) with either of the two compounds known to reduce Miro1, Benidipine (Figures 1-2, S2) and Miro1 Reducer 3 (MR3) (Hsieh et al., 2019; Li et al., 2021). Miro1 protein levels upon CCCP

treatment were lowered by each compound in all 4 patients (Figure 7G), showing that the Miro1 marker in PBMCs can respond to drug treatment. Collectively, our results suggest that Miro1 protein in blood cells may be used to aid in diagnosis and drug development.

Rare variants in the iron-calcium-Miro pathway are associated with PD status

After dissecting the functional impairment of this iron-calcium-Miro axis in PD, we explored its genetic contribution to PD. Earlier, we showed that chelating iron, blocking Miro's binding to Ca^{2+}, or preventing Ca^{2+}-entry into the cell all alleviated parkinsonian neurodegeneration (Figures 2, 3, 7). We evaluated genes encoding the protein targets of these approaches, which are spatially distinct and localized to three subcellular locations: (1) IMM Ca^{2+}-channels and transporters (targeted by Fe^{2+}), (2) the Ca^{2+}-binding protein Miro on the OMM, and (3) plasma membrane Ca^{2+}-channels (targeted by Benidipine and Tranilast) (Figure 7H, Table S5). By analyzing common variants within or near any of the investigated genes in GWAS reported in (Nalls et al., 2019), we did not observe significant association with PD clinical status. We next employed the whole-genome sequencing (WGS) data from the Accelerating Medicines Partnership–Parkinson's Disease (AMP–PD) (1,168 control; 2,241 PD), and assessed rare non-synonymous and damaging variants using burden based and SKATO methods. We discovered polygenetic vulnerability to PD at all three spatial hotspots: significant association with PD status of rare variants in selective T-type Ca^{2+}-channel subtypes (*Cav3.2*, *3.3*) (cell surface), *Miro2* (OMM), and *NCLX* (IMM) (Table S5). A SKATO Test on all variants of T-type or L-type Ca^{2+}-channel subtypes consistently showed significant association with PD status of T-type channels, which survived multiple comparison correction, but not of L-type channels (Table S5). Together, our analysis discovers genetic predisposition of this Ca^{2+}-pathway to PD.

To functionally validate the selection of T-type Ca^{2+}-channels from our human genetic study, we employed the same screening ICC assay described earlier (Figures S1-2) by which we discovered the non-selective pan-Ca^{2+}-channel blocker, Benidipine, but now using 2 different specific L-type and 3 different T-type Ca^{2+}-channel blockers. Intriguingly, we again discovered a striking selection of T-type versus L-type channels, in the connection with Miro1 in PD fibroblasts (Figure S7G): only T-type blockers promoted Miro1 degradation following depolarization, just like Benidipine, supporting the human genetic finding. Similar to Miro1, Miro2 was also resistant to depolarization-triggered degradation in PD fibroblasts (Hsieh et al., 2019) and responded to Benidipine treatment (Figure S3C). NCLX functionally interacts with MCU (Lee et al., 2016), and was coregulated with MCUb and MCU by Fe^{2+} (Figure 5F, 6B, S5) and PD (Figure 7E). Although it remains elusive why rare variants in these genes are selectively associated with PD, our combined, unbiased analyses of human genetics, tissues, cell, and in vivo models corroborate the complexity and multifactorial nature of PD etiology, and indicate that the polygenetic architecture built around this iron-calcium-Miro axis might influence an individual's risk to develop PD.

Discussion

In this work, we have established a pathway of iron-calcium-Miro dysregulation in our PD models (Figure 7H). Elevation of iron concentrations may cause mitochondrial Ca^{2+}-overload by promoting the MCU activity and reducing NCLX levels (Figures 4-7, S5). It is possible that the initial mitochondrial Ca^{2+}-accumulation subsequently disrupts Ca^{2+}-homeostasis at the cellular level, eliciting responses of additional Ca^{2+}-binding proteins, such as Miro (Figure 7H). We have shown multiple ways to target this axis. Chelating iron, reducing Ca^{2+}-entry into the cell, or blocking Miro's binding to Ca^{2+} is each neuroprotective

(Figures 2, 3, 7). Of note, the impairment of this axis can be reflected in blood cells using a Miro1 assay with high content capacity (Figure 7F-G) and can be detected in the genome of PD patients (Table S5). Hence, this ionic axis may be important for PD pathogenesis and can be leveraged for better detecting and treating the disease.

Although the precise course of PD pathogenesis remains unclear, emerging evidence has demonstrated its complex and polygenetic nature. Interactions among multiple organs and cell types, systemic immune activation, and environmental triggers act uniquely in different individuals. Although GWAS and segregation studies have unveiled many PD risk or causal loci, rare genetic variants may be particularly important for conferring individual heterogeneity in disease onset and etiology. However, rare variants associated with PD risk are difficult to discover given the limitations in sample collection and the unmet need for exome-sequencing as opposed to sparse genotyping on microarrays. In our work, we have located several potential risk genes by first connecting them in the same biological pathway. In an individual prone to PD, there might be already mitochondrial malfunction causing mitochondrial proteins to release labile iron inside the mitochondria, or impairments in systemic iron uptake and circulation causing iron accumulation at the cellular level. Any predisposed genetic perturbations in this iron-calcium-Miro axis, which could be due to different rare variants in each person, would further exacerbate its dysfunction. With or without another trigger such as a virus infection or environmental insult, the tipping point for disease onset might be reached. Thus, combining complementary genetic and functional studies may help us better understand the destructive paths leading to the disease and identify network hubs for therapeutic targeting.

Screening people for genetic variants in this iron-calcium-Miro axis and detecting Miro in blood cells may help stratify a unique population of patients and at-risk individuals, who will particularly benefit from therapeutic interventions targeting this axis. For example, treating people bearing genetic variants in Ca^{2+}-channels with Ca^{2+}-channel blockers, iron-chelators, or both, may yield the best efficacy. Similarly, people who test positive for the Miro1 phenotype in PBMCs may respond best to drugs reducing Miro1. Integrating genetic screening of this axis with Miro1 detection in peripheral tissues may enhance the accuracy of risk evaluation and help design personalized treatment, such as a cocktail of different Ca^{2+}-channel blockers, iron chelators, and Miro reducers, to improve prevention and treatment efficacy.

Calcium mishandling and iron accumulation have been widely observed in PD neurons (Angelova et al., 2020; Apicco et al., 2021; Belaidi and Bush, 2016; Buttner et al., 2013; Kim et al., 2020; Lee et al., 2018; Surmeier et al., 2017; Tabata et al., 2018; Verma et al., 2017; Vuuren et al., 2020). Now we have provided a mechanistic link. Fe^{2+} elicits mitochondrial Ca^{2+}-overload through acting on IMM Ca^{2+}-channels and transporters. Further investigations are needed to dissect how Fe^{2+} regulates MCUb and NCLX levels. One hypothesis is that these proteins are targeted by Ca^{2+}-activated mitochondrial proteases. Our results (Figure 6I) have suggested that Fe^{2+}-triggered Ca^{2+}-efflux delay depends on mitochondrial Ca^{2+}-overload. A recent study has shown that NCLX protein levels are lowered in another mitochondrial iron-dependent disease, Friedreich's Ataxia (FA), through a possible mechanism dependent on calpain cleavage (Britti et al., 2021). Intriguingly, iron chelators have displayed promising therapeutic benefits in preclinical models of both PD (Clark et al., 2020) and FA (Llorens et al., 2019), and is currently in multiple clinical trials for treating symptoms of PD patients (Clark et al.,

2020). Thus, the underlying molecular mechanisms may be shared by multiple diseases with mitochondrial iron accumulation.

The consequences to intracellular Ca^{2+}-dysfunction could be profound and detrimental. Dissecting these downstream details in PD will help us find more powerful targets and biomarkers. Mitochondrial Ca^{2+}-overload could overwhelm the oxidative phosphorylation system (Ashrafi et al., 2020), damaging the electron transport chain. Malfunctions of MCU and NCLX may disrupt spatially discrete Ca^{2+} transients and oscillations adjacent to ER membranes, leading to defects in autophagy (Zheng et al., 2022), which may consequently cause protein aggregation and lysosomal dysfunction. Intriguingly, chelating iron can induce selective autophagy pathways (Wilhelm et al., 2022), raising the question whether MCU and local Ca^{2+} dynamics are involved in iron-mediated autophagy. Ca^{2+} may be also important for safeguarding mitochondrial quality. Miro appears to be a molecular switch between distinct routes of mitochondrial quality control. Proteasomal degradation of Miro dissociates mitochondria from microtubules and allows the entire damaged mitochondria to enter the mitophagy pathway (Chan et al., 2011; Hsieh et al., 2016; Wang et al., 2011), whereas sustaining Miro on the microtubule motors is required for the biogenesis of mitochondrial derived vesicles (MDVs) that deliver a subset of mitochondrial proteins (including Miro) to lysosomes (Konig et al., 2021). Notably, MDVs occur under mild oxidative stress or at steady state, and before mitophagy which is triggered by extended damage (Konig et al., 2021; Lin et al., 2017; McLelland et al., 2014). Miro may also ride with those damaged mitochondria expelled from neurons through nanotunnels and vesicles (Ahmad et al., 2014; Davis et al., 2014; Melentijevic et al., 2017; Rosina et al., 2022; Saha et al., 2022). Perhaps it starts with only one of these biological processes impaired by Ca^{2+} signals, leading to Miro retention on damaged mitochondria, which further affects more Miro-dependent quality control pathways. More studies are needed to unravel the precise roles of Miro and other Ca^{2+}-binding proteins in PD pathogenesis and how Ca^{2+} regulates these roles. The physical and functional interactions of these Ca^{2+}-binding proteins with specific Ca^{2+}-channels in plasma, mitochondrial, or additional organellar membranes, may constitute the core underlying mechanisms.

Data availability

Further information and reagents are available from the corresponding author.

Acknowledgements

We thank M.F. Tsai for *MCU* KO cells, L. Pallanck for flies, A. E. Medlock, O. Ross, and S. Han for discussion, C. Kwak, Z. T. Cook, D. M. Conradson and J. Panji for technical support, the Steinberg lab for assistance, the Wang lab members for discussion, the Stanford HTBC (RRID: SCR_017794) and D. E. Solow-Cordero for assistance with drug screens, and the SBC, the Stanford Alzheimer's Disease Research Center (ADRC), the Department of Pathology at University of California Los Angeles (UCLA), R. N. Alcalay, Columbia University, and the Michael J. Fox Foundation (MJFF) for providing human tissues and cells. This work was supported by NINDS (RO1NS089583, RO1NS128040-01; X.W.), NIGMS (RO1GM143258; X.W.), NIA (RO1AG060747; M.D.G.), Stanford SPARK and Spectrum SPADA (X.W.), Sanofi iAward (X.W.), the Warren Alpert Foundation (X.W.), the MJFF (021146; X.W.), the Harrington Discovery Institute (X.W.), the Belgian American Education Foundation (R.V.), the Glenn Foundation Postdoctoral Fellowship (L.L.), and the European Union's Horizon 2020 research and innovation program under the Marie Skłodowska-Curie (890650; Y.LG.).

Author contributions

R.V. did drug screens. S.E.R. and R.B.A. performed pathway analysis. V.B., A.S.D., C.-H.H., L.L., and S.C. performed human cell experiments. L.L. conducted fly work. C.M.M. and L.F. did in vitro work. Y.LG. and M.D.G. analyzed human genetic data. P.N. analyzed PBMC data. X.W. conceived and supervised the project. All authors designed the experiments and wrote the paper.

Competing interests

The authors declare the following competing interests: X.W. is a co-founder, adviser, and shareholder of AcureX Therapeutics, and a shareholder of Mitokinin Inc. V.B., L.L., C.-H.H., and R.V. are shareholders of AcureX Therapeutics. P.N. is employed by Vroom Inc. Patents based on this study were filed by Stanford University with X.W., R.V., V.B., L.L., C.-H.H. as inventors. The remaining authors declare no competing interests.

REFERENCES

Ahmad, T., Mukherjee, S., Pattnaik, B., Kumar, M., Singh, S., Kumar, M., Rehman, R., Tiwari, B.K., Jha, K.A., Barhanpurkar, A.P., *et al.* (2014). Miro1 regulates intercellular mitochondrial transport & enhances mesenchymal stem cell rescue efficacy. The EMBO journal *33*, 994-1010.

Angelova, P.R., Choi, M.L., Berezhnov, A.V., Horrocks, M.H., Hughes, C.D., De, S., Rodrigues, M., Yapom, R., Little, D., Dolt, K.S., *et al.* (2020). Alpha synuclein aggregation drives ferroptosis: an interplay of iron, calcium and lipid peroxidation. Cell death and differentiation *27*, 2781-2796.

Apicco, D.J., Shlevkov, E., Nezich, C.L., Tran, D.T., Guilmette, E., Nicholatos, J.W., Bantle, C.M., Chen, Y., Glajch, K.E., Abraham, N.A., *et al.* (2021). The Parkinson's disease-associated gene ITPKB protects against alpha-synuclein aggregation by regulating ER-to-mitochondria calcium release. Proceedings of the National Academy of Sciences of the United States of America *118*.

Ashrafi, G., de Juan-Sanz, J., Farrell, R.J., and Ryan, T.A. (2020). Molecular Tuning of the Axonal Mitochondrial Ca(2+) Uniporter Ensures Metabolic Flexibility of Neurotransmission. Neuron *105*, 678-687 e675.

Baughman, J.M., Perocchi, F., Girgis, H.S., Plovanich, M., Belcher-Timme, C.A., Sancak, Y., Bao, X.R., Strittmatter, L., Goldberger, O., Bogorad, R.L., *et al.* (2011). Integrative genomics identifies MCU as an essential component of the mitochondrial calcium uniporter. Nature *476*, 341-345.

Belaidi, A.A., and Bush, A.I. (2016). Iron neurochemistry in Alzheimer's disease and Parkinson's disease: targets for therapeutics. Journal of neurochemistry *139 Suppl 1*, 179-197.

Billesbolle, C.B., Azumaya, C.M., Kretsch, R.C., Powers, A.S., Gonen, S., Schneider, S., Arvedson, T., Dror, R.O., Cheng, Y., and Manglik, A. (2020). Structure of hepcidin-bound ferroportin reveals iron homeostatic mechanisms. Nature *586*, 807-811.

Britti, E., Delaspre, F., Tamarit, J., and Ros, J. (2021). Calpain-Inhibitors Protect Frataxin-Deficient Dorsal Root Ganglia Neurons from Loss of Mitochondrial Na(+)/Ca(2+) Exchanger, NCLX, and Apoptosis. Neurochem Res *46*, 108-119.

Buttner, S., Faes, L., Reichelt, W.N., Broeskamp, F., Habernig, L., Benke, S., Kourtis, N., Ruli, D., Carmona-Gutierrez, D., Eisenberg, T., *et al.* (2013). The Ca2+/Mn2+ ion-pump PMR1 links elevation of cytosolic Ca(2+) levels to alpha-synuclein toxicity in Parkinson's disease models. Cell death and differentiation *20*, 465-477.

Chan, N.C., Salazar, A.M., Pham, A.H., Sweredoski, M.J., Kolawa, N.J., Graham, R.L., Hess, S., and Chan, D.C. (2011). Broad activation of the ubiquitin-proteasome system by Parkin is critical for mitophagy. Human molecular genetics *20*, 1726-1737.

Clark, E.H., Vazquez de la Torre, A., Hoshikawa, T., and Briston, T. (2020).

Targeting mitophagy in Parkinson's disease. The Journal of biological chemistry.
Darakhshan, S., and Pour, A.B. (2015). Tranilast: a review of its therapeutic applications. Pharmacol Res *91*, 15-28.
Davis, C.H., Kim, K.Y., Bushong, E.A., Mills, E.A., Boassa, D., Shih, T., Kinebuchi, M., Phan, S., Zhou, Y., Bihlmeyer, N.A., *et al.* (2014). Transcellular degradation of axonal mitochondria. Proceedings of the National Academy of Sciences of the United States of America *111*, 9633-9638.
Diaz-Ortiz, M.E., Seo, Y., Posavi, M., Carceles Cordon, M., Clark, E., Jain, N., Charan, R., Gallagher, M.D., Unger, T.L., Amari, N., *et al.* (2022). GPNMB confers risk for Parkinson's disease through interaction with alpha-synuclein. Science *377*, eabk0637.
Dong, Z., Shanmughapriya, S., Tomar, D., Siddiqui, N., Lynch, S., Nemani, N., Breves, S.L., Zhang, X., Tripathi, A., Palaniappan, P., *et al.* (2017). Mitochondrial Ca(2+) Uniporter Is a Mitochondrial Luminal Redox Sensor that Augments MCU Channel Activity. Molecular cell *65*, 1014-1028 e1017.
Fan, C., Fan, M., Orlando, B.J., Fastman, N.M., Zhang, J., Xu, Y., Chambers, M.G., Xu, X., Perry, K., Liao, M., *et al.* (2018). X-ray and cryo-EM structures of the mitochondrial calcium uniporter. Nature *559*, 575-579.
Fan, M., Zhang, J., Tsai, C.W., Orlando, B.J., Rodriguez, M., Xu, Y., Liao, M., Tsai, M.F., and Feng, L. (2020). Structure and mechanism of the mitochondrial Ca(2+) uniporter holocomplex. Nature *582*, 129-133.
Ghosh, S., Basu Ball, W., Madaris, T.R., Srikantan, S., Madesh, M., Mootha, V.K., and Gohil, V.M. (2020). An essential role for cardiolipin in the stability and function of the mitochondrial calcium uniporter. Proceedings of the National Academy of Sciences of the United States of America *117*, 16383-16390.
Hsieh, C.H., Li, L., Vanhauwaert, R., Nguyen, K.T., Davis, M.D., Bu, G., Wszolek, Z.K., and Wang, X. (2019). Miro1 Marks Parkinson's Disease Subset and Miro1 Reducer Rescues Neuron Loss in Parkinson's Models. Cell metabolism *30*, 1131-1140 e1137.
Hsieh, C.H., Shaltouki, A., Gonzalez, A.E., Bettencourt da Cruz, A., Burbulla, L.F., St Lawrence, E., Schule, B., Krainc, D., Palmer, T.D., and Wang, X. (2016). Functional Impairment in Miro Degradation and Mitophagy Is a Shared Feature in Familial and Sporadic Parkinson's Disease. Cell stem cell *19*, 709-724.
Kim, J.W., Yin, X., Jhaldiyal, A., Khan, M.R., Martin, I., Xie, Z., Perez-Rosello, T., Kumar, M., Abalde-Atristain, L., Xu, J., *et al.* (2020). Defects in mRNA Translation in LRRK2-Mutant hiPSC-Derived Dopaminergic Neurons Lead to Dysregulated Calcium Homeostasis. Cell stem cell *27*, 633-645 e637.
Konig, T., Nolte, H., Aaltonen, M.J., Tatsuta, T., Krols, M., Stroh, T., Langer, T., and McBride, H.M. (2021). MIROs and DRP1 drive mitochondrial-derived vesicle biogenesis and promote quality control. Nature cell biology.
Lambert, J.P., Luongo, T.S., Tomar, D., Jadiya, P., Gao, E., Zhang, X., Lucchese, A.M., Kolmetzky, D.W., Shah, N.S., and Elrod, J.W. (2019). MCUB Regulates the Molecular Composition of the Mitochondrial Calcium Uniporter Channel to Limit Mitochondrial Calcium Overload During Stress. Circulation *140*, 1720-1733.
Lee, K.S., Huh, S., Lee, S., Wu, Z., Kim, A.K., Kang, H.Y., and Lu, B. (2018). Altered ER-mitochondria contact impacts mitochondria calcium homeostasis and contributes to neurodegeneration in vivo in disease models. Proceedings of the National Academy of Sciences of the United States of America *115*, E8844-E8853.
Lee, S.K., Shanmughapriya, S., Mok, M.C.Y., Dong, Z., Tomar, D., Carvalho, E., Rajan, S., Junop, M.S., Madesh, M., and Stathopulos, P.B. (2016). Structural Insights into Mitochondrial Calcium Uniporter Regulation by Divalent Cations. Cell Chem Biol *23*, 1157-1169.
Li, L., Conradson, D.M., Bharat, V., Kim, M.J., Hsieh, C.H., Minhas, P.S., Papakyrikos, A.M., Durairaj, A.S., Ludlam, A., Andreasson, K.I., *et*

al. (2021). A mitochondrial membrane-bridging machinery mediates signal transduction of intramitochondrial oxidation. Nat Metab.
Lin, M.Y., Cheng, X.T., Tammineni, P., Xie, Y., Zhou, B., Cai, Q., and Sheng, Z.H. (2017). Releasing Syntaphilin Removes Stressed Mitochondria from Axons Independent of Mitophagy under Pathophysiological Conditions. Neuron *94*, 595-610 e596.
Lin, Y.F., Cheng, C.W., Shih, C.S., Hwang, J.K., Yu, C.S., and Lu, C.H. (2016). MIB: Metal Ion-Binding Site Prediction and Docking Server. J Chem Inf Model *56*, 2287-2291.
Llorens, J.V., Soriano, S., Calap-Quintana, P., Gonzalez-Cabo, P., and Molto, M.D. (2019). The Role of Iron in Friedreich's Ataxia: Insights From Studies in Human Tissues and Cellular and Animal Models. Front Neurosci *13*, 75.
Lu, C.H., Lin, Y.F., Lin, J.J., and Yu, C.S. (2012). Prediction of metal ion-binding sites in proteins using the fragment transformation method. PloS one *7*, e39252.
McLelland, G.L., Soubannier, V., Chen, C.X., McBride, H.M., and Fon, E.A. (2014). Parkin and PINK1 function in a vesicular trafficking pathway regulating mitochondrial quality control. The EMBO journal *33*, 282-295.
Melentijevic, I., Toth, M.L., Arnold, M.L., Guasp, R.J., Harinath, G., Nguyen, K.C., Taub, D., Parker, J.A., Neri, C., Gabel, C.V.*, et al.* (2017). C. elegans neurons jettison protein aggregates and mitochondria under neurotoxic stress. Nature *542*, 367-371.
Munson, M.J., Mathai, B.J., Ng, M.Y.W., Trachsel-Moncho, L., de la Ballina, L.R., Schultz, S.W., Aman, Y., Lystad, A.H., Singh, S., Singh, S.*, et al.* (2021). GAK and PRKCD are positive regulators of PRKN-independent mitophagy. Nature communications *12*, 6101.
Nalls, M.A., Blauwendraat, C., Vallerga, C.L., Heilbron, K., Bandres-Ciga, S., Chang, D., Tan, M., Kia, D.A., Noyce, A.J., Xue, A.*, et al.* (2019). Identification of novel risk loci, causal insights, and heritable risk for Parkinson's disease: a meta-analysis of genome-wide association studies. The Lancet Neurology *18*, 1091-1102.
Nguyen, D., Bharat, V., Conradson, D.M., Nandakishore, P., and Wang, X. (2021). Miro1 Impairment in a Parkinson's At-Risk Cohort. Front Mol Neurosci *14*, 734273.
Ordureau, A., Paulo, J.A., Zhang, J., An, H., Swatek, K.N., Cannon, J.R., Wan, Q., Komander, D., and Harper, J.W. (2020). Global Landscape and Dynamics of Parkin and USP30-Dependent Ubiquitylomes in iNeurons during Mitophagic Signaling. Molecular cell *77*, 1124-1142 e1110.
Palty, R., Silverman, W.F., Hershfinkel, M., Caporale, T., Sensi, S.L., Parnis, J., Nolte, C., Fishman, D., Shoshan-Barmatz, V., Herrmann, S.*, et al.* (2010). NCLX is an essential component of mitochondrial Na+/Ca2+ exchange. Proceedings of the National Academy of Sciences of the United States of America *107*, 436-441.
Patron, M., Tarasenko, D., Nolte, H., Kroczek, L., Ghosh, M., Ohba, Y., Lasarzewski, Y., Ahmadi, Z.A., Cabrera-Orefice, A., Eyiama, A.*, et al.* (2022). Regulation of mitochondrial proteostasis by the proton gradient. The EMBO journal *41*, e110476.
Rosina, M., Ceci, V., Turchi, R., Chuan, L., Borcherding, N., Sciarretta, F., Sanchez-Diaz, M., Tortolici, F., Karlinsey, K., Chiurchiu, V.*, et al.* (2022). Ejection of damaged mitochondria and their removal by macrophages ensure efficient thermogenesis in brown adipose tissue. Cell Metab.
Saha, T., Dash, C., Jayabalan, R., Khiste, S., Kulkarni, A., Kurmi, K., Mondal, J., Majumder, P.K., Bardia, A., Jang, H.L.*, et al.* (2022). Intercellular nanotubes mediate mitochondrial trafficking between cancer and immune cells. Nat Nanotechnol *17*, 98-106.
Shaltouki, A., Hsieh, C.H., Kim, M.J., and Wang, X. (2018). Alpha-synuclein delays mitophagy and targeting Miro rescues neuron loss in Parkinson's models. Acta Neuropathol *136*, 607-620.

Shchepinova, M.M., Cairns, A.G., Prime, T.A., Logan, A., James, A.M., Hall, A.R., Vidoni, S., Arndt, S., Caldwell, S.T., Prag, H.A., *et al.* (2017). MitoNeoD: A Mitochondria-Targeted Superoxide Probe. Cell Chem Biol *24*, 1285-1298 e1212.
Surmeier, D.J., Obeso, J.A., and Halliday, G.M. (2017). Selective neuronal vulnerability in Parkinson disease. Nature reviews Neuroscience *18*, 101-113.
Tabata, Y., Imaizumi, Y., Sugawara, M., Andoh-Noda, T., Banno, S., Chai, M., Sone, T., Yamazaki, K., Ito, M., Tsukahara, K., *et al.* (2018). T-type Calcium Channels Determine the Vulnerability of Dopaminergic Neurons to Mitochondrial Stress in Familial Parkinson Disease. Stem cell reports *11*, 1171-1184.
Tomar, D., Dong, Z., Shanmughapriya, S., Koch, D.A., Thomas, T., Hoffman, N.E., Timbalia, S.A., Goldman, S.J., Breves, S.L., Corbally, D.P., *et al.* (2016). MCUR1 Is a Scaffold Factor for the MCU Complex Function and Promotes Mitochondrial Bioenergetics. Cell Rep *15*, 1673-1685.
Verma, M., Callio, J., Otero, P.A., Sekler, I., Wills, Z.P., and Chu, C.T. (2017). Mitochondrial Calcium Dysregulation Contributes to Dendrite Degeneration Mediated by PD/LBD-Associated LRRK2 Mutants. The Journal of neuroscience : the official journal of the Society for Neuroscience *37*, 11151-11165.
Vuuren, M.J.V., Nell, T.A., Carr, J.A., Kell, D.B., and Pretorius, E. (2020). Iron Dysregulation and Inflammagens Related to Oral and Gut Health Are Central to the Development of Parkinson's Disease. Biomolecules *11*.
Wang, X., and Schwarz, T.L. (2009). The mechanism of Ca2+ -dependent regulation of kinesin-mediated mitochondrial motility. Cell *136*, 163-174.
Wang, X., Winter, D., Ashrafi, G., Schlehe, J., Wong, Y.L., Selkoe, D., Rice, S., Steen, J., LaVoie, M.J., and Schwarz, T.L. (2011). PINK1 and Parkin target Miro for phosphorylation and degradation to arrest mitochondrial motility. Cell *147*, 893-906.
Wilhelm, L.P., Zapata-Munoz, J., Villarejo-Zori, B., Pellegrin, S., Freire, C.M., Toye, A.M., Boya, P., and Ganley, I.G. (2022). BNIP3L/NIX regulates both mitophagy and pexophagy. The EMBO journal, e111115.
Zheng, Q., Chen, Y., Chen, D., Zhao, H., Feng, Y., Meng, Q., Zhao, Y., and Zhang, H. (2022). Calcium transients on the ER surface trigger liquid-liquid phase separation of FIP200 to specify autophagosome initiation sites. Cell.

FIGURE LEGENDS

Figure 1. HTP Screens Identify Ca^{2+}-Related Drug Hits for PD. (A) Schematic representation of a custom-designed drug screen for Miro1 in PD fibroblasts. (B) Pathway analysis identified calcium as a shared factor in the primary hit-Miro1 network. Each individual pathway is generated using a primary hit and Miro1 as search query and the resulting subnetwork is visualized and curated using docs2graph–a knowledge-graph browser. The visualization shows a subgraph generated by docs2graph from the collection of curated supporting documents for each pathway.

Figure 2. Benidipine Rescues PD Relevant Phenotypes. (A-B) iPSC-derived neurons from a PD patient with *SNCA-A53T* and the isogenic control, treated as indicated, were immunostained with anti-TH (A) or TUNEL and Dapi (B), and imaged under a confocal microscope. Scale bars: 100 μm. Below: Quantifications of the density of TH-positive neurons (A) or the percentage of TUNEL-positive neurons (B). n=20 images from 3 independent coverslips. P values are compared with the far-left bar, except indicated otherwise. (C) 40-day-old fly brains were immunostained with anti-TH and the DA neuron number was counted in the PPL1 cluster. Scale bar: 20 μm. n=4, 7, 7, 4 (from left to right). (D) The Performance Index was measured in 30-day-old flies, fed as indicated. n=59, 57, 54, 57 flies (from left to

right), 3 independent experiments. (C-D) Drug treatment was started from adulthood (day 1). One-Way Anova Post Hoc Tukey Test for all panels.

Figure 3. The EF-hands of Miro Play a Role in Causing PD Relevant Phenotypes. (A) Representative still images from live Mito-dsRed and GFP-Miro1 imaging movies of axons of indicated genotypes, following 100 μM Antimycin A treatment. Scale bar: 10 μm. (B) Left: Quantification of the GFP-Miro1 intensity at 25 minutes divided by that at 0 minute following 100 μM Antimycin A treatment from the same axonal region. Right: Quantification of the reduction speed of the GFP-Miro1 intensity within 25 minutes following 100 μM Antimycin A treatment. (C) Left: Quantification of the Mito-dsRed intensity at 58 minutes divided by that at 0 minute following 100 μM Antimycin A treatment from the same axonal region. Right: Quantification of the Mito-dsRed intensity reduction speed within 58 minutes following 100 μM Antimycin A treatment. (B-C) n=5, 4, 5 (from left to right) axons (one axon per coverslip). (D) The DA neuron number was counted in the PPL1 cluster of flies with indicated genotypes. Scale bar: 20 μm. n=7, 4, 6, 5 (from left to right). (E) The Performance Index was measured in flies with indicated genotypes and age. n (from left to right)=49, 47, 40, 47 flies (day 12); 49, 47, 39, 47 (day 14); 48, 45, 37, 44 (day 20); 3 independent experiments. One-Way Anova Post Hoc Tukey Test for all panels.

Figure 4. PD Mitochondria Accumulate Ca^{2+}, Fe^{2+}, and ROS. (A) iPSC-derived neurons from a PD patient with *SNCA-A53T* and the isogenic control were stimulated with thrombin and mitochondrial (Rhod-2) and cytosolic Ca^{2+} levels (Calcium Green) were measured. Left: Representative traces of Ca^{2+} ions in neurons. Right: Quantifications of the peak fluorescent intensity normalized to baseline. n=15 cell bodies from 3 independent coverslips. (B) Left: Confocal single section images of live neurons as in (A) stained with RPA (mitochondrial Fe^{2+}–Mito-Fe^{2+}) and MitoTracker Green (Mito-Green). Right: Quantifications of the RPA fluorescent intensity normalized to MitoTracker Green. n=26 (WT) and 28 (PD) cell bodies from 3 coverslips. (C) Left: Confocal single section images of live neurons stained with MitoNeoD and MitoTracker Green (Mito-Green). Right: Quantifications of the MitoNeoD fluorescent intensity normalized to MitoTracker Green. n=25 cell bodies from 3 coverslips. Two-tailed Welch's T Test for all panels. Scale bars: 10 μm.

Figure 5: Iron Promotes MCU Oligomerization. (A-D) HEK cells were treated as indicated and run through SEC. Fractions were run in SDS-PAGE and blotted. (E) Elution profiles for (A-D). (F) HEK cells were treated similarly as above, run in Native-PAGE, and blotted. Below: Qualifications of the band intensities normalized to the total protein amount measured by BCA. n=5 independent experiments. One-Way Anova Post Hoc Tukey Test.

Figure 6. MCU Binds to Fe^{2+}. (A) HEK cells were treated with or without 5 mM Fe^{2+} for 21 hours, then IPed with rabbit IgG or anti-MCU, and Fe^{2+} concentrations in the IP samples were detected. n=4 independent experiments. Top western blots demonstrated the success of IP. Anti-MCU was validated using *MCU-/-* HEK cell lysate (bottom panel). Arrow indicates the MCU band. (B) HEK cells were treated with 5 mM Fe^{2+} or Co^{2+} for 22 hours and lysed in buffer containing the same metal. Lysates were run in Native- or SDS-PAGE and blotted with anti-MCU. Similar results were seen for at least 3 times. (C) HEK cells treated with 5 mM Fe^{2+} or 500 μM Co^{2+} for 22 hours were stimulated with thrombin and mitochondrial Ca^{2+} levels (Rhod-2) were measured. The peak fluorescent intensity normalized to baseline is quantified. n=20 cells from 4 independent coverslips. (D-E) Fluorescence-detection SEC profiles of purified human MCU. The annotation of the peaks is based on (Fan et al., 2018; Fan et al., 2020). (F) Left: Representative blots of IP with anti-Flag using cell lysates as indicated, run in Native- or SDS-PAGE.

Right: Quantification of the band intensity of MCU-Flag in Native-PAGE normalized to that in SDS-PAGE from the same experiment. n=4 independent experiments. (G) HEK cells treated as indicated were stimulated with thrombin and mitochondrial Ca^{2+} levels (Rhod-2) were measured. Representative traces of Ca^{2+} ions. (H-I) Based on traces like in (G), the peak fluorescent intensity normalized to baseline (H) or efflux rate (I) is quantified. n=17 cells from 4 independent coverslips. Two-tailed Welch's T Test for all panels.

Figure 7. Chelating Iron Restores Ca^{2+} and neuronal homeostasis in PD neurons. (A) Similar to Figure 4A, iPSC-derived neurons from a PD patient with *SNCA-A53T* and the isogenic control, with or without treatment of 100 μM DFP for 24 hours, were stimulated with thrombin, and mitochondrial Ca^{2+} (Rhod-2) was measured. Quantifications of the peak fluorescent intensity normalized to baseline. n=15 cell bodies from 3 independent coverslips. Control data without DFP treatment are the same as in Figure 4A. One-Way Anova Post Hoc Tukey Test. (B) iPSC-derived neurons treated as indicated, were immunostained with TUNEL and Dapi, and imaged under a confocal microscope. Scale bar: 50 μm. Below: Quantification of the percentage of TUNEL-positive neurons. n=20 images from 3 independent coverslips. P values are compared within each genotype (significant compared to every other condition) with One-Way Anova Post Hoc Tukey Test. (C) The DA neuron number was counted in the PPL1 cluster of flies with indicated genotypes and conditions. Drug treatment was started from adulthood (day 1). Scale bar: 20 μm. n=6, 9, 8, 7 (from left to right). (D) The Performance Index was measured in flies. Drug treatment was started from embryogenesis. n=35, 33, 40, 34 flies (from left to right), 3 independent experiments. (C-D) One-Way Anova Post Hoc Tukey Test. (E) Postmortem brains were run in Native- or SDS-PAGE and blotted. The band intensity normalized to the total protein level measured by BCA is divided by that of the universal control on the same blot: CVD (cardiovascular disease), which was included on every blot. The MCU oligomer bands in Native-PAGE and the NCLX and MCUb bands in SDS-PAGE (average of 3 replicates) are used in the plot. HC: healthy control. (F) Miro1 protein levels were measured using ELISA in PBMCs treated with DMSO or 40 μM CCCP for 6 hours. Miro1 Ratio is calculated by dividing the Miro1 value treated with CCCP by that with DMSO from the same subject. Dot plot with Mean±S.E.M. n=80 healthy controls and 107 PD. Two-tailed Welch's T Test. (G) PBMCs from 4 PD patients were treated with 40 μM CCCP for 6 hours, or pretreated with 10 μM Benidipine or MR3 for 18 hours and then with 40 μM CCCP for another 6 hours, and Miro1 protein was detected using ELISA. Patient IDs are the same as in Table S4. Two-tailed paired T Test. (H) Schematic representation of the iron-calcium-Miro axis discovered in this study. Red texts show genes containing variants associated with PD.

METHODS

Subject Details of Human Cells and Tissues

No human subjects were used in this study. The iPSC work was approved by the Stanford Stem Cell Oversight Committee. iPSCs and fibroblasts were purchased under a material transfer agreement (MTA) from the NINDS Human Cell and Data Repository, which is in a partnership with multiple institutions that deposited cells, approved study protocols, ensured consent from donors, and explained the conditions for donating materials for research. PBMCs were obtained under an MTA with Columbia University and the MJFF, and from the SBC and the Stanford ADRC. Postmortem brain tissues were obtained from the Stanford ADRC and the Department of Pathology at UCLA. Columbia University, Stanford University, and UCLA Institutional Review Board approved study protocols, which ensured consent from donors and explained the conditions for donating materials for research. Demographic and clinical details of each subject are in Supplementary Tables.

Constructs

pcDNA3.1-MCU-Flag (MCU_OHu20308D_pcDNA3.1+/C-(K)-DYK) was purchased from Genescript. pcDNA3.1-MCU-3A-Flag was generated by making 3 point-mutations (74D, 148D, 159H to A) of MCU_OHu20308D_pcDNA3.1+/C-(K)-DYK. pRK5-GFP-hMiro1-WT or KK was custom-made by Synbio Technologies. pDsRed2-Mito was from Clontech. pUAST-T7-DMiro-KK was generated by introducing E234K, E354K to pUAST-T7-DMiro (Tsai et al., 2014).

Cell Culture

Human dermal primary fibroblasts isolated from a PD patient (ND39528) and a healthy control (ND36091) were cultured in DMEM (11995-065, Thermo Fisher) supplemented with 10% fetal bovine serum (900-108, heat-inactivated, Gemini Bio-Products), 1×Anti Anti (15240096, Thermo Fisher), and 1×GlutaMax (35050061, Thermo Fisher) maintained in a 37°C, 5% CO_2 incubator with humidified atmosphere. Cells were treated with 10 μM Benidipine (B6813, Sigma-Aldrich) for 30 hours, or 40 μM CCCP (C2759, Sigma-Aldrich) for 6 hours. HEK293T cells were cultured in DMEM (11995-065, Thermo Fisher) supplemented with 10% fetal bovine serum (900-108, heat-inactivated, Gemini Bio-Products), 1% Pen-Strep (15140-122, Gibco), and maintained in a 37°C, 5% CO_2 incubator with humidified atmosphere.

iPSC Culture, Differentiation, and Transfection

All iPSC lines in this study are summarized below and have been fully characterized by our previous studies (Hsieh et al., 2016; Shaltouki et al., 2018), and the NINDS Human Cell and Data Repository.

iPSC line	Source	Etiology	PD mutation	Age	Sex
PD-I	NINDS (ND50050); Episomal reprogramming	Genetic	*SNCA (A53T)*	51	Female
PD-II	NINDS (ND39896)	Sporadic	*Unknown*	77	Male
Wild-type-I	NINDS (ND50085)	Isogenic control for *PD-I*	*Wild-type*	51	Female
Wild-type-II	Hsieh et al., 2016	Healthy Control	*Wild-type*	62	Male

iPSCs were derived to midbrain DA neurons as previously described with minor modifications (Byers et al., 2011; Hsieh et al., 2016; Kriks et al., 2011; Nguyen et al., 2011; Wichterle et al., 2002). Briefly, neurons were generated using an adaptation of the dual-smad inhibition method. Neural induction was

started when iPSCs reached 50-85% confluency, with the use of dual smad inhibitors, dorsormorphin (P5499, Sigma-Aldrich) and TGFβ inhibitor SB431542 (1614, Tokris), and the addition of GSK3β inhibitor CHIR99021 (04-0004, Stemgent) and smoothened agonist SAG (566661, CalBioChem). To get single cell, 12 days after neural induction, half of the medium was replaced with N2 medium with 20 ng ml^{-1} BDNF (450-02, Peprotech), 200 μM ascorbic acid (A5960, Sigma-Aldrich), 500 nM SAG, and 100 ng ml^{-1} FGF8a (4745-F8-050, R&D Systems). On day 16-17, neurons were split and transferred onto Matrigel (354277, Corning)-coated or poly-ornithine and laminin-coated glass coverslips in a 24-well plate. On day 19-20, medium was switched to N2 medium supplemented with 20 ng ml^{-1} BDNF, 200 μM ascorbic acid, 20 ng ml^{-1} GDNF (450-10, Peprotech), 1 ng ml^{-1} TGFβ3 (AF-100-36E, Peprotech), and 500 μM dibutyryl-cAMP (D0627, Sigma-Aldrich) for maturation of DA neurons. Neurons were used at day 21-23 after neuronal induction, when about 80-90% of total cells expressed the neuronal marker TUJ-1, and 12-19% of total cells expressed TH and markers consistent with ventral midbrain neuronal subtypes (Sanders et al., 2014; Shaltouki et al., 2018).

For transfection, on day 19-20 after neural induction, culture medium was replaced with Opti-MEM (Gibco) prior to transfection. 0.5-1 μg DNA or 1-5 μl Lipofectamine 2000 (11668-030, Invitrogen) was diluted in Opti-MEM at room temperature (22°C) to a final volume of 50 μl in two separate tubes, and then contents of the two tubes were gently mixed, incubated for 20 minutes at room temperature, and subsequently added onto neurons. After 6 hours, Opti-MEM containing DNA-Lipofectamine complexes was replaced with regular N2 medium with supplements. After transfection for 2-3 days, neurons were used.

Neurons were treated with 50-100 μM DFP (HY-B0568, MedChemExpress) for 24 hours, 10 μM Benidipine (B6813, Sigma-Aldrich) for 30 hours, 10 μM Antimycin A (A8674, Sigma-Aldrich) for 6 hours, or 100 μM Antimycin A during live imaging.

Primary Drug Screens

Overall scheme: Fibroblasts were plated and cultured for 24 hours. Compound libraries were then applied for 10 hours. Next, 20 μM FCCP was added for another 14 hours. FCCP is a mitochondrial uncoupler that depolarizes the mitochondrial membrane potential and triggers Miro1 degradation and the following mitophagy (Birsa et al., 2014). Application of mitochondrial uncouplers has been successfully used in high-throughput screens searching for genes and chemicals in the mitophagy pathway (Clark et al., 2020; Hiroyuki Katayama, 2020; Hoshino et al., 2019). After fixation, cells were stained with anti-Miro1 and 4',6-diamidino-2-phenylindole, dihydrochloride (Dapi), and imaged under the confocal microscope with the identical setting (Figure 1A). Anti-Miro1 has been validated in ICC for specifically recognizing endogenous Miro1 using human fibroblast-derived neurons with *Miro1* RNAi (Hsieh et al., 2016). The Miro1 intensity was normalized to Dapi from those images. Using this analysis, we observed significant Miro1 reduction following FCCP treatment in fibroblasts from a healthy control subject but not in a sporadic PD fibroblast line (Figure S3A), consistent with our previous studies using the same cell lines by Western blotting or ELISA (Hsieh et al., 2019). We then employed this method to screen 3 chemical libraries (NIH, FDA, and Sigma) using the PD cell line. The NIH Clinical collection library contains 377 unique compounds. We screened those drugs at a defined concentration of 10 μM with 4 biological repeats for each drug. We compared calculated Miro1 levels in PD cells treated with both compound and FCCP to those treated with FCCP but without any compound. We found that 11 out of 377 unique compounds reduced Miro1 protein levels following FCCP treatment below the standard deviation of control Miro1 values (those from the same PD cell line without compound treatment but with FCCP), in all biological

repeats (Figure S1A, Table S1A) (Ehrenkaufer et al., 2018). We next screened the Biomol FDA library with five-fold doses (1.25, 2.5, 5, 10, 20 μM) in duplicate. From 175 unique compounds, we identified 3 hits that reduced Miro1 protein levels following FCCP treatment in a dose-dependent manner (Figure S1B, Table S1A). Lastly, we screened the Sigma LOPAC library which contains 1269 unique compounds at a defined concentration of 20 μM. We found that 21 compounds reduced Miro1 protein levels below the standard deviation of those control Miro1 values from the same PD cell line without compound treatment (Figure S1C, Table S1A). We ranked all hits in the order of the degree of Miro1 reduction (Table S1A). It is important to note that from the same screens we also identified compounds that enhanced Miro1 protein levels in PD cells treated with FCCP (Table S1B). Although our purpose was to search for Miro1 reducers in PD models, the same assay could be used to look for Miro1 enhancers in other disease models.

Method details: Fibroblasts were plated onto clear-bottomed/black-walled 384-well plates (EK-30091, E&K Scientific) at 2,000 cells/well with a Matrix Wellmate dispenser (Thermo Fisher), and plates were incubated at 37°C, 5% CO_2 for 24 hours. Next, chemical library compounds at defined concentrations were added using fully automated liquid handling system (Caliper Life Sciences Staccato system) with a Twister II robot and a Sciclone ALH3000 (Caliper Life Sciences) integrated with a V&P Scientific pin tool, and plates were incubated at 37°C, 5% CO_2 for 10 hours. Then, 20 μM of FCCP (C2920, Sigma-Aldrich) was added to wells and plates were incubated at 37°C, 5% CO_2 for another 14 hours. Cells were fixed with ice-cold 90% methanol (482332, Thermo Fisher) for 20 minutes at -20°C, then incubated with blocking buffer (10% normal goat serum–50062Z, Thermo Fisher; 0.5% BSA–BP1600, Thermo Fisher; 0.2% Triton X-100–T8787, Thermo Fisher) at room temperature for 15 minutes, and incubated with anti-Miro1 (HPA0101687, Sigma-Aldrich) at 1:100 in blocking buffer overnight at 4°C. Samples were washed with 1×PBS (10010-049, Thermo Fisher) using a Plate Washer multivalve (ELx405UV, Bio-Tek), incubated with goat anti-Rabbit IgG (H+L) Cross-Adsorbed, Alexa Fluor 488 (A11008, Thermo Fisher) at 1:500 in blocking buffer at 25°C for 2 hours, then washed again with 1×PBS, and finally 1.0 μg/ml Dapi (D1306, Thermo Fisher) in 1×PBS was added and plates were sealed using PlateLoc (01867.001, Velocity11). All liquids were dispensed using the Multidrop 384 (5840200, Titertek) unless otherwise stated. Fluorescent signals in plates were automatically imaged with ImageXpress Micro (Molecular Devices, IXMicro) and data were analyzed with MetaXpress Analysis (Molecular Devices). One image was taken from one well. Our negative controls without primary anti-Miro1 generated no Miro1 signals. Only cells positive for both Miro1 and Dapi staining were chosen for analysis (>99%; total 400-600 cells per image). The Miro1 fluorescent intensity was normalized to that of Dapi from the same cell and averaged across all cells from the image from one well. Then, the median of the mean Miro1 intensities of all wells from the same plate was calculated and subtracted from the mean Miro1 intensity of each well.

Retesting Hits from the Primary Screens

Overall scheme: We didn't test 1 hit (CV-3988) because it was unavailable for purchase at the time of the experiments. We applied each of the 34 compounds at the highest screening concentration to the same sporadic PD line used at the HTBC with at least 4 biological replicates. We also evaluated Miro1 protein levels without FCCP but with compound treatment, which unveiled the drug effect on Miro1 under the basal condition in PD fibroblasts. We imaged all samples with the identical imaging setting, and our negative controls without primary anti-Miro1 yielded almost no signals (background; Table S1C). Four compounds, A-77636 hydrochloride, Ebselen, GBR-12909 dihydrochloride and Fenbufen, appeared toxic (Table S1C). We found that 15 out of the initial 34 hit compounds consistently reduced Miro1 protein following FCCP treatment below the standard deviation of control Miro1 values (those from the same PD cell line without treatment) (Figure S2A-B, Table S1C). In summary, we discovered 15 compounds in two

independent experimental settings that reduced Miro1 protein levels following mitochondrial depolarization in PD fibroblasts (Figure S2C).

Method details: Fibroblasts were plated on coverslips (22-293232, Fisher scientific) into 24-well plates (10861-558, VWR) at 20,000 cells/well and plates were incubated at 37°C, 5% CO_2 for 24 hours. Next, fresh chemical compounds dissolved in DMSO were added at defined concentrations and plates were incubated at 37°C, 5% CO_2 for 10 hours. Then, FCCP at 20 μM was added to wells and plates were incubated at 37°C, 5% CO_2 for another 14 hours. Cells were fixed with ice-cold 90% methanol for 20 minutes at -20°C, incubated with blocking buffer (10% normal goat serum, 0.5% BSA, 0.2% Triton X-100) at 25°C for 15 minutes, and immunostained with anti-Miro1 (HPA0101687, Sigma-Aldrich) at 1:100 in blocking buffer overnight at 4°C. Samples were washed three times with 1×PBS, incubated with goat anti-Rabbit IgG (H+L) Cross-Adsorbed, Alexa Fluor 488 (A11008, Thermo Fisher) at 1:500 in blocking buffer at 25°C for 2 hours, washed again three times with 1×PBS, and finally samples were mounted with ProLong™ Glass Antifade Mountant with NucBlue™ (Dapi) Stain (P36983, hard-setting, Thermo Fisher) on glass slides and allowed to cure overnight. Samples were imaged at 25°C with a 20×/N.A.0.60 oil Plan-Apochromat objective on a Leica SPE laser scanning confocal microscope (JH Technologies), with identical imaging parameters among different genotypes. Three images were taken per coverslip. Total 4 biological repeats (coverslips) for each drug. Images were processed with ImageJ (Ver. 1.48, NIH), and the average Miro1 intensity in the cytoplasmic area was measured using the Intensity Ratio Nuclei Cytoplasm Tool (http://dev.mri.cnrs.fr/projects/imagej-macros/wiki/Intensity_Ratio_Nuclei_Cytoplasm_Tool). All compound information for retesting is in Table S1C or in Figure S7.

Pathway Analysis

Putative mechanistic pathways were generated using graph search over a network of over 2 million relationships between chemicals, diseases, and genes extracted from the abstracts of journal publications deposited in PubMed (Percha and Altman, 2018). Each chemical hit and Miro1 were used as the source and target inputs for a weighted shortest path algorithm where paths were only allowed to traverse chemical-gene and gene-gene relationships. Graph search over the biomedical graph was performed using Neo4J. A subnetwork associated with each shortest path was generated from its supporting documents and analyzed using a knowledge graph browser (docs2graph) to curate the set of supporting documents.

Immunocytochemistry and Confocal Microscopy

Adult fly brains were dissected in PBST (0.3% Triton X-100 in PBS) and incubated with fixative solution (4% formaldehyde in PBST) for 15 minutes at room temperature. Fixed samples were incubated in blocking solution (10% BSA in PBST) for an hour, and then immunostained with rabbit anti-TH (AB-152, EMD Millipore) at 1:200 in blocking solution for 36 hours at 4°C on a rotator. After wash, donkey anti-rabbit 488 (ab175470, Abcam) at 1:1000 was applied in blocking solution for 1 hour at room temperature in dark. The DA neuron number was counted throughout the Z stack images of each brain. Representative images were summed stack images.

Human neurons were fixed in 4% paraformaldehyde (Electron Microscopy Sciences, Hatfield, PA) for 15 minutes at room temperature, permeabilized with 0.25% Triton X-100 in PBS for 20 minutes, then washed twice in PBS (5 minutes each) and rinsed in deionized water. Alexa Fluor 594 picolyl azide based TUNEL assay was performed according to the manufacturer's instruction (C10618, Invitrogen). Coverslips were incubated with TdT reaction buffer at 37°C for 10 minutes, followed by TdT reaction mixture at 37°C for

60 minutes in a humidified chamber. Coverslips were then rinsed with deionized water, washed with 3% BSA and 0.1% Triton X-100 in PBS for 5 minutes, followed by incubation with Click-iT plus TUNEL reaction cocktail at 37°C for 30 minutes, and then washed with 3% BSA and 0.1% Triton X-100 in PBS for 5 minutes. For nuclear counterstain, 4', 6-Diamidino-2-phenylindole (Dapi; D9542, Sigma-Aldrich) at 0.5 μg/ml was applied at room temperature for 10 minutes in the dark. The coverslips were washed with PBS twice, and then mounted on slides with Fluoromount-G mounting medium (SouthernBiotech). For some experiments, Dapi was stained with ProLong™ Glass Antifade Mountant with NucBlue™ Stain (P36983, hard-setting, Thermo Fisher). Or iPSC-derived neurons were fixed in 4% paraformaldehyde for 15 minutes, washed twice in PBS (5 minutes each), and then blocked in PBS with 5% normal goat serum and 0.3% Triton X-100 for 60 minutes. Neurons were then immunostained with rabbit anti-TH (AB-152, EMD Millipore) at 1:500 in antibody buffer (PBS with 1% BSA and 0.3% Triton X-100) at 4°C overnight, followed by Alexa Fluor 488 fluorochrome conjugated goat anti-rabbit IgG (A11008, Invitrogen) at 1:500 in antibody buffer at room temperature for 1 hour. Coverslips were washed with PBS twice, and then mounted on slides with Fluoromount-G mounting medium. Samples were imaged at room temperature with a 20×/N.A.0.60 or 63×/N.A.1.30 oil Plan-Apochromat objective on a Leica SPE laser scanning confocal microscope, with identical imaging parameters among different genotypes in a blinded fashion. Images were processed with ImageJ (Ver. 1.48, NIH) using only linear adjustments of contrast and color.

Live Cell Imaging

MitoNeoD at 5 μM (563761, MedKoo Biosciences Inc.), RPA at 5 μM (ME043.1, Squarix biotechnology), MitoTracker Green at 75 nM (M7514, Thermo Fisher), or TMRM at 25 nM (T668, Molecular Probes) was applied to cells on coverslips in culture media at 37°C for 30 minutes, then coverslips were washed with Hanks Balanced Salt Solution (HBSS) and each placed in a 35-mm petri-dish containing Hibernate E low-fluorescence medium (HELF, BrainBits/Transnetyx), and cells were imaged immediately on a heated stage of 37°C with a 63/N.A.0.9 water-immersion objective. For calcium imaging, Rhod-2 (R1244, Thermo Fisher) and Calcium Green (C3011MP, Thermo Fisher) at 5 μM were applied to cells on coverslips and incubated at 37°C for 30 minutes with the same set-up as above. Thrombin (10602400001, Sigma-Aldrich) was applied at 100 mUnits/ml to the dish during imaging. Time-lapse movies were obtained continually with a 2 second interval for 8-10 minutes. For Mito-dsRed and GFP-Miro1 imaging, live neurons were imaged as above and time-lapse movies were obtained continually with a 1 second interval before and after 100 μM Antimycin (A8674, Sigma-Aldrich) addition.

Fly Work

The following fly stocks were used: *Actin-GAL4* (Bloomington Drosophila Stock Center–BDSC), *TH-GAL4* (BDSC), *UAS-SNCA*^{A53T} (Trinh et al., 2008), and *UAS-T7-DMiro-WT* (Tsai et al., 2014). *UAS-T7-DMiro-KK* were generated by injecting pUAST-T7-DMiro-KK into flies by Bestgene Inc (Chino Hills, CA). All fly stocks and experiments were kept at 25°C with a 12:12 hrs light:dark cycle and constant humidity (65%) on standard sugar-yeast-agar (SYA) medium (15 g/l agar, 50 g/l sugar, 100 g/l autolyzed yeast, 6 g/l nipagin, and 3 ml/l propionic acid) (Castillo-Quan et al., 2016). Flies were raised at standard density in 200 ml bottles unless otherwise stated. All fly lines were backcrossed 6 generations into a w^{1118} background to ensure a homogeneous genetic background. The ages of flies for each experiment were stated in Figures. Experiments were carried out on mated females (Sofola et al., 2010).

DFP (HY-B0568, MedChemExpress) was dissolved in water at 50 mM and added to SYA fly food at a final concentration of 163 μM. Benidipine (B6813, Sigma-Aldrich) was dissolved in DMSO at 10 mM and added to SYA fly food at a final concentration of 2.5 μM. The same volume of solvent was added to

control food. Drug treatment was started on newly-eclosed mated females (day 1), except for DFP on locomotion which was started from embryogenesis. Food was refreshed every 2 days.

The average Performance Index (PI) (negative geotaxis) was evaluated as previously described (Kinghorn et al., 2015; Rival et al., 2004; Sofola et al., 2010). Briefly, adult flies were gently tapped to the base of a modified 25 ml climbing tube and their climbing progress was recorded after 45 seconds. Two to four populations of flies were assessed, and for each population, flies were examined 3 times per experiment. The recorded values were used to calculate the average PI.

Western Blotting and IP

In general, lysates for SDS-PAGE were mixed with 4×Laemmli sample buffer (161-0747, Bio-Rad) containing 5-10% β-mercaptoethanol, and then boiled for 5 minutes before being loaded into either a precast 10% polyacrylamide gel (4561034, Bio-Rad) or manually made gel for electrophoresis with Tris-glycine-SDS running buffer (24.8 mM Tris, 192 mM glycine, 0.1% SDS). For Native-PAGE, cells were lysed in lysis buffer (300 mM NaCl, 50 mM Tris pH 7.5, 1% Triton X-100, 0.5% Digitonin, 5 mM EDTA, 0.2 mM PMSF, Protease Inhibitor Cocktail–P8340, Sigma-Aldrich), and centrifuged at 16,200 g 4°C for 1 hour. Lysates were mixed with 2×Native Tris-Glycine sample buffer (LC2673, Life Technologies) and loaded directly into a precast 10% polyacrylamide gel (4561034, Bio-Rad) with Tris-glycine Native running buffer (24.8 mM Tris, 192 mM glycine). After electrophoresis, nitrocellulose membranes (1620115, Bio-Rad) were used in semi-dry transfer with Bjerrum Schafer–Nielsen buffer (48 mM Tris, 39 mM glycine, 20% methanol (v/v), pH 9.2). Transferred membranes were first blocked in TBST (TBS with 0.01-0.05% Tween-20) with 5% milk for 1 hour at room temperature, and then immunoblotted with the following primary antibodies in TBST with 5% milk at 4°C overnight: mouse anti-Miro1 (WH0055288M1, Sigma-Aldrich) at 1:1,000, rabbit anti-GAPDH (5174 S, Cell Signaling Technology) at 1:1,000, rabbit anti-MCU (HPA016480, Sigma-Aldrich) at 1:500, rabbit anti-Flag (F7425, Sigma-Aldrich) at 1:750-1,000, rabbit anti-NCLX (ab136975, Abcam) at 1:1,000, rabbit anti-MCU (26312-1-AP, Proteintech) at 1:1,000, rabbit anti-Miro2 (14016S, Cell Signaling Technology) at 1:1,000, mouse anti-ATP5β (ab14730, Abcam) at 1:1,000, rabbit anti-MCUb (AP12355b, Abgent) at 1:1,000, rabbit anti-β-Actin (4967S, Cell Signaling Technology) at 1:1,000, rabbit anti-Mitofusin2 (9482S, Cell Signaling Technology) at 1:1,000, mouse anti-MIC60 (ab110329, Abcam) at 1:500, mouse anti-MIC19 (TA803454, Origene) at 1:1,000, rabbit anti-MICU1 (HPA037479, Sigma-Aldrich) at 1:1,000, rabbit anti-MICU2 (ab101465, Abcam) at 1:1,000, rabbit anti-FECH (14466-1-AP, Proteintech) at 1:500, rabbit anti-EMRE (HPA032117, Sigma-Aldrich) at 1:500, rabbit anti-OPA1 (80471S, Cell Signaling Technology) at 1:1,000, mouse anti-T7 (69622, Novagen) at 1:1,000, and rabbit anti-VDAC (4661S, Cell Signaling Technology) at 1:1,000. Secondary HRP-conjugated goat anti-rabbit or mouse IgG antibodies (Jackson ImmunoResearch Laboratories) were used at 1:3,000–10,000 for 1 hour at room temperature. West Dura ECL Reagent (34075, GE Healthcare) or SuperSignal™ West Pico PLUS Chemiluminescent Substrate (Thermo fisher scientific) was added. Membranes were scanned using a Bio-Rad ChemiDoc XRS system.

HEK cells (0.3×10^6/well in a 6-well plate) were plated, grown overnight, and next day when 30-40% confluent, transfected with 1 μg of DNA, using the calcium phosphate transfection protocol. After 24 hours of transfection, media was changed. After 48 hours of transfection, cells were treated without or with Fe^{2+} (5 mM, Ammonium Iron(II) Sulfate Hexahydrate, 203505, Sigma-Aldrich) for 24 hours followed by lysing with 300 μl of lysis buffer (300 mM NaCl, 50 mM Tris pH 7.5, 1% Triton X-100, 0.2 mM PMSF, Protease Inhibitor Cocktail) supplemented with 5 mM EDTA or 5 mM Fe^{2+}. For each condition, 3 wells of a 6-well plate were pooled, followed by centrifugation at 16,200 g for 10 minutes at

4°C. Part of the supernatant (110 µl out of 900 µl total) was reserved as 'Input'. The remaining 790 µl was incubated with 10 µl of anti-Flag (F7425, Sigma-Aldrich) for 2 hours on a rotator at 4°C, and then combined with 60 µl of washed Protein A–Sepharose beads (17-0780-01, GE Healthcare) for 1 hour on a rotator at 4°C. Beads were then washed five times with lysis buffer. Residual buffer was removed from the last wash and the beads were mixed with 100 µl of 2×Tris-Glycine Native Sample Buffer (LC2673, Thermo Fisher) or Laemmli buffer (then boiled), and loaded into a precast gel (4561034, Bio-Rad). For each gel running, approximately 5% (45 µl out of total 900 µl lysate) of total lysates (Input) and 45% of total immunoprecipitated proteins were loaded.

Postmortem Brain Analysis

A piece of postmortem brain (1 mm^3) was cut and put in a 1.5 ml tube, and lysed in 500 µl of lysis buffer (300 mM NaCl, 50 mM Tris pH 7.5, 1% Triton X-100, 0.5% Digitonin, 5 mM EDTA, Protease Inhibitor Cocktail, 0.2 mM PMSF). Tissue was sonicated and then centrifuged at 16,200 g 4°C for 1 hour. Supernatant was collected.

RT-qPCR

Total RNA was extracted from at least one million cells per sample using TRIzol (Gibco) according to the manufacturer's instructions. Concentrations of total RNA were measured using a NanoDrop. 1 µg of total RNA was then subjected to DNA digestion using DNase I (Ambion), immediately followed by reverse transcription using the iScript Reverse Transcription Supermix (1708841, BIO-RAD). qPCR was performed using the StepOnePlus™ instrument (Thermo Fisher) and SYBR Green Supermix (172-5270, Bio-Rad) following the manufacturer's instructions. Human *GAPDH* was amplified as an internal standard. Expression levels were analyzed by the StepOne Software (Version 2.2.2). The relative expression level of *Miro1* was divided by that of *GAPDH* from the same experiment. Each experiment was repeated 4 times in duplicate. The following primers were used:
GAPDH forward: 5'- ACCACAGTCCATGCCATCAC-3'
GAPDH reverse: 5'- TCCACCACCCTGTTGCTGT-3'
Miro1 forward: 5'- GGGAGGAACCTCTTCTGGA-3'
Miro1 reverse: 5'- ATGAAGAAAGACGTGCGGAT-3'

ATP Levels

ATP concentrations were determined using the Roche ATP Bioluminescence Assay Kit HS II (no. 11699709001, Sigma). Briefly, cell lysate was homogenized in 150 µl of ice-cold lysis buffer as above using a Kontes pellet pestle. Lysate was then boiled for 5 minutes and centrifuged at 20,000 g 4°C for 1 minute. Cleared lysate was diluted 1:200 in dilution buffer and loaded with 10 µl of luciferase. Luminescence was immediately measured using a FlexStation 3 (Molecular Devices). Total protein amounts were measured using the Bicinchoninic Acid (BCA) Protein Assay Kit (23227, Thermo Scientific). The ATP level in each sample was normalized to the total protein amount.

SEC

For control and H_2O_2 treatment (10 mM for 10 minutes), HEK cells were lysed in lysis buffer (1% Triton X-100, 50 mM Tris pH7.5, 300 mM NaCl, 5 mM EDTA, 1:1000 Protease inhibitor cocktail, 0.2 mM PMSF). For Fe^{2+} treatment, HEK cells were treated with 5 mM Fe^{2+} (Ammonium Iron(II) Sulfate Hexahydrate, 203505, Sigma-Aldrich) for 24 hours, and lysed in the same buffer above where EDTA was replaced with 5 mM Fe^{2+}. For Ca^{2+} treatment, HEK cells were lysed in the same buffer above where EDTA was replaced with 2 mM Ca^{2+}. Cell lysates were injected onto a Superdex 200 Increase 10/300 GL column

(GE Healthcare Life Sciences). To slow Fe^{2+}-oxidation and precipitation in equilibration buffer, we preequilibrated the column with low pH buffer and reducing reagent. For the control sample, the column was preequilibrated with 20 mM MES pH 6.0, 300 mM NaCl, 5 mM TCEP, and 0.1% Triton X-100. For the Fe^{2+}-treated sample, the column was preequilibrated with 20 mM MES pH 6.0, 300 mM NaCl, 5 mM TCEP, 2 mM Fe^{2+}, and 0.1% Triton X-100. For the Ca^{2+} and H_2O_2-treated sample, the column was preequilibrated with 20 mM Tris pH 7.4, 300 mM NaCl, and 0.1% Triton X-100.

Fluorescence SEC: For each sample, 5 µg purified human MCU was incubated either on ice or at 35°C in a thermal cycler for 15 minutes. After the incubation, all samples were centrifuged in a tabletop centrifuge at 21,000 g at 4°C for 10 minutes to remove precipitated protein. The supernatant was then injected onto a Superdex 200 Increase 10/300 GL column preequilibrated with 20 mM Tris pH 7.4, 150 mM NaCl, 0.01% lauryl maltose neopentyl glycol (LMNG), and 0.001% cholesteryl hemisuccinate (CHS).

Iron Detection

HEK cells from one well of a 6-well plate were lysed in 120 µl lysis buffer (1% Triton X-100, 50 mM Tris pH7.5, 300 mM NaCl, 5 mM EDTA, 1:1000 Protease inhibitor cocktail, 0.2 mM PMSF), and 3 wells were pooled for each IP, followed by centrifugation at 16,200 g 4°C for 10 minutes. For Fe^{2+} treatment, HEK cells were treated with 5 mM Fe^{2+} (Ammonium Iron(II) Sulfate Hexahydrate, 203505, Sigma-Aldrich) for 21 hours, and lysed in the same buffer where EDTA was replaced with 5 mM Fe^{2+}. Supernatant was then incubated with 7 µl rabbit anti-MCU (26312-1-AP, ProteinTech) or rabbit IgG (2729S, cell signaling) for 3 hours at 4°C, and incubated with Protein A–Sepharose beads (17-0780-01, GE Healthcare) for another hour at 4°C. To detect iron levels, the colorimetric iron detection assay kit (ab83366, Abcam) was used according to the manufacturer's instruction. Briefly, 180 µl Iron Assay Buffer was added to the beads with IP, and 100 µl of mixed buffer-beads was added to each well of total 2 wells. Next, 5 µl Iron Reducer was added to the well for iron (II+III), and 5 µl of Iron Assay Buffer was added to the well for iron (II), incubated at 37°C for 30 minutes. Then, 100 µl Iron Probe was added to each well, incubated at 37°C for 60 minutes, protected from light. Samples were measured immediately by an InfiniteM200 Pro TECAN plate reader at 593 nm.

PMBC Analysis

PBMCs were thawed in a 37°C water bath and plated into a 6-well plate (353046, Falcon) with RPMI media (11875-093, Gibco), supplemented with 10% fetal bovine serum (900-108, heat-inactivated, Gemini Bio-Products), 1% Pen-Strep (15140-122, Gibco), 1×GlutaMax (35050061, Thermo Fisher), and maintained in a 37°C, 5% CO_2 incubator with humidified atmosphere. After a 1-hour recovery in the incubator, cells were then trypsinized with 0.25% Trypsin-EDTA (25200-056, Gibco) and collected in a cell suspension to be counted via TC20 Cell Counter (Bio-Rad).

For Western blotting: After counting, the cell suspension (total 8 million cells) was equally split into 8 groups and replated with 3 ml media per well, 2 groups remaining untreated (to serve as controls), 3 groups treated with a combination of 20 µM Antimycin A (A8674, Sigma-Aldrich) and 2 µM Oligomycin (75351, Sigma-Aldrich) (AO), and 3 groups treated with 40 µM CCCP (C2759, Sigma-Aldrich). The untreated groups, serving as the 0-hour treatment in a time course, were then immediately pelleted and lysed with 150 µl lysis buffer (1% Triton X-100, 50 mM Tris, 300 mM NaCl, 5 mM EDTA, 0.2 mM PMSF, 1:1,000 Protease Inhibitor Cocktail) and stored at -80°C. At each of the following time points after treatment – 1 hour, 6 hours, and 14 hours – 1 group from each of the treatments (AO or CCCP) was similarly pelleted, lysed with lysis buffer, and stored at -80°C. Lysates collected were run in SDS-PAGE (30 µl loaded) and

blotted with the following primary antibodies: mouse anti-Miro1 (WH0055288M1, Sigma-Aldrich) at 1:1,000, rabbit anti-GAPDH (5174 S, Cell Signaling Technology) at 1:1,000, mouse anti-ATP5β (ab14730, Abcam) at 1:1,000, rabbit anti-VDAC (4661S, Cell Signaling Technology) at 1:1,000, and rabbit anti-β-Actin (4967S, Cell Signaling Technology) at 1:1,000.

For ELISA: After counting, the cell suspension was equally split and replated with 3 ml media per well containing either 40 μM CCCP or a commensurate volume of DMSO for 6 hours. PBMC vials were provided in duplicate by the MJFF, so the cell suspensions did not need to be split equally – they kept separate throughout the counting and replating process. For PBMCs that received drug treatment, the cell suspension was equally split into 3 wells. One well was pretreated with 10 μM Benidipine or MR3 (1915758622, MCULE) for 18 hours, and then this well and a second well were treated with 40 μM CCCP for 6 hours. The same volume of DMSO was applied to control wells. The minimum cell number needed for ELISA was 400,000 per well. Next, cells were scraped gently with a cell lifter and collected into suspension. The cells were then pelleted and lysed with lysis buffer (1% Triton X-100, 50 mM Tris, 300 mM NaCl, 5 mM EDTA, 0.2 mM PMSF, 1:1,000 Protease Inhibitor Cocktail) and stored at -80°C. The Miro1 protein level in each sample collected was determined using the RHOT1 ELISA Kit 96T (EKL54911, Biomatik) according to the manufacturer's manual, and normalized to the total protein level in the same sample using the BCA Protein Assay Kit (23227, Thermo Scientific). OD values for ELISA and BCA were measured on an InfiniteM200 Pro TECAN plate reader at 450 and 562 nm respectively, in duplicate. All experiments were performed in a double-blinded fashion, with PD status unknown to the experimenter.

Human Genetics

Based on our experimental data showing the importance of the calcium-Miro axis in PD models, the following calcium related genes were investigated for genetic association: *CACNA1S, CACNA1C, CACNA1D, CACNA1B, CACNA1G, CACNA1H, CACNA1I, RHOT1, RHOT2, MCU, CCDC109B, MICU1, MICU2, SMDT1, SLC8B1, TRPV1, TRPV2, TRPV3, TRPV4* (Table S5). First, to identify whether common variants regulating the expression (eQTL) or splicing (sQTL) of these genes are associated with PD risk, we queried the genome-wide association study (GWAS) summary statistics from (Nalls et al., 2019). Genome-wide significant association (if any) was then intersected with eQTL/sQTL information from GTEx (Consortium et al., 2017). Due to the absence of association, colocalization was not formally tested. Second, to test the association of rare variants in these genes we performed Burden and SKATO Test, as implemented in the R package *SKAT* v2.2.4, considering variants with a CADD (Combined Annotation Dependent Depletion) score (Rentzsch et al., 2019) above 20 to only include variants most likely to have an impact on protein function. Additionally, we grouped variants in *CAC* genes by channel type, particularly grouping T-type (*CACNA1G, CACNA1H, CACNA1I*) and L-type (*CACNA1S, CACNA1C, CACNA1D*). For rare variant analysis, we obtained whole-genome sequencing (WGS) data from the Accelerating Medicines Partnership–Parkinson's Disease (AMP–PD), composed of the following cohorts: New Discovery of Biomarkers (BioFIND), the Harvard Biomarker Study (HBS), the Parkinson's Progression Markers Initiative (PPMI) (Nalls et al., 2016), and the Parkinson's Disease Biomarkers Program (PDBP). European ancestry individuals and principal components to account for genetic ancestry were computed as described in (Le Guen et al., 2021), leading to a total of 1,168 controls (45.4% males) and 2,241 cases (62.8% males). Significance was assessed separately for Burden and SKATO Test, though in genes where deleterious missense variants were all associated with the phenotype in the same direction (either increasing or decreasing risk) these two tests led to similar results. Due to the relatively small

sample sizes, we reported nominally significant results in the text and did not account for multiple comparisons, unless otherwise stated.

Machine Learning

We trained a machine learning model to classify if a patient was with PD or not. The general form of the logistic regression model was represented by the following equation:

$$p(C_1|x) = \frac{1}{e^{-(\beta_0+\sum_{i=1}^{N}\beta_i x_i)}}$$

The goal of the model training was to learn the model parameters β_i such that we could predict the posterior probability $p(C_1|x)$. C_1 represented the positive class "PD+" status and x represented the input of the model. We set a threshold value above which all predictions belonged to the positive class, i.e., "PD+", and below which they belonged to the "PD-" class.

We trained three logistic regression models with three different inputs. The first model used "Miro1 Ratio" as the only input, the second one had "UPDRS" as the only input, and the third model combined "Miro1 Ratio" and "UPDRS" as inputs. All three models were trained using the glm function in R.

We broke the total subjects into a 60% training set and a 40% testing set. Data was cleaned by converting assigning column values to appropriate data types and omitting rows of data where no "Miro1 Ratio" or "UPDRS" values were present. The target variable, PD status, was labeled and encoded where 0 represented a subject without PD and 1 represented a PD positive subject.

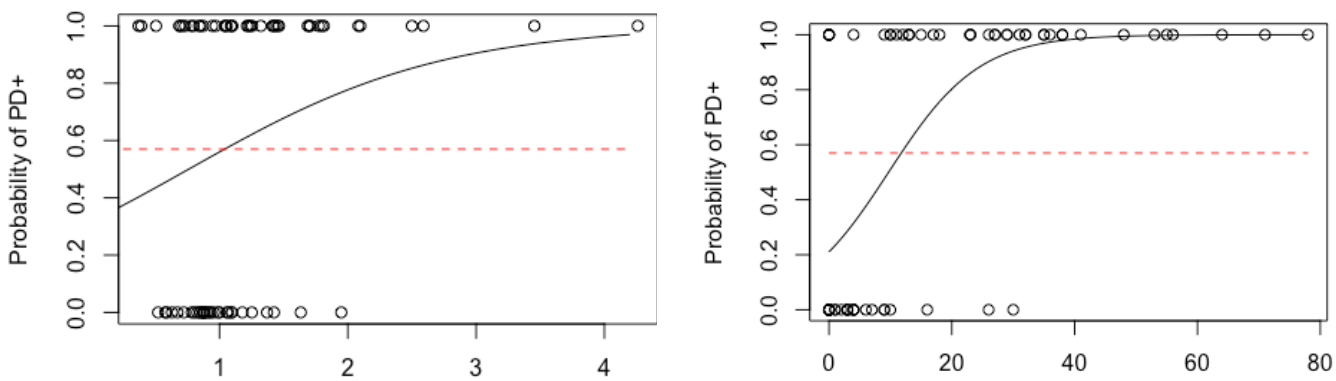

Left panel showed the trained model for the probability of "PD+" with "Miro1 Ratio" as the only feature. The decision boundary for the probability was set to 0.57. This value maximized the accuracy and AUC score for this model. Above this threshold all predictions were considered as "PD+" and the ones below were considered as "PD-". Right panel showed the trained model for "UPDRS". Please note that in both figures the probability of "PD+" was not zero when Input was zero.

The table below showed the β_i and the corresponding p-values.

Model	features	Estimate	Std Error	z.value	Pr
Miro1 Ratio only	(Intercept)	-0.76541	0.500231	-1.5301	0.125991
	Miro1_Ratio	1.006977	0.460706	2.185727	0.028836
UPDRS only	(Intercept)	-1.32384	0.340155	-3.89189	0.0000995
	UPDRS	0.13644	0.027073	5.039669	4.66E-07
Miro1 Ratio + UPDRS	(Intercept)	-3.45836	1.030444	-3.35618	0.00079

Model	features	Estimate	Std Error	z.value	Pr
	UPDRS	0.193639	0.062998	3.073723	0.002114
	Miro1_Ratio	2.002893	0.863175	2.320378	0.02032
	UPDRS:Miro1_Ratio	-0.04647	0.048114	-0.96573	0.334178

The estimate column represented β_i for each model. Since the "Miro1 Ratio" only and the "UPDRS" only models had a single feature, there were only two β_i values present. β_0 represented the intercept and β_1 represented "Miro1 Ratio" value or the "UPDRS" value depending on the model. We observed that the β_i estimate for the Miro1 Ratio model was significant ($p<0.05$) suggesting that the model predictions were statistically significant. Similarly, for UPDRS the β_1 value was also significant. Both the UPDRS and Miro1 Ratio estimates were significant in the combined model, however the interaction term between them was non-significant.

Once the models were trained, they were tested by evaluating the accuracy and AUC scores. The table below presented the accuracy and AUC scores for all models:

Models	Accuracy	AUC
Miro1 Ratio only	0.676	0.677
UPDRS only	0.812	0.822
Miro1 Ratio + UPDRS	0.878	0.878

We observed that the Miro1 Ratio only model performed worse with an accuracy of 67.6% than the UPDRS only model (81.2%). However, together it yielded a higher score of 87.8%.

We then added "Age" and "Sex" as additional inputs to the combined mode which did not affect the accuracy.

Code is in supporting material.

References

Birsa, N., Norkett, R., Wauer, T., Mevissen, T.E., Wu, H.C., Foltynie, T., Bhatia, K., Hirst, W.D., Komander, D., Plun-Favreau, H., *et al.* (2014). Lysine 27 ubiquitination of the mitochondrial transport protein Miro is dependent on serine 65 of the Parkin ubiquitin ligase. The Journal of biological chemistry *289*, 14569-14582.

Byers, B., Cord, B., Nguyen, H.N., Schule, B., Fenno, L., Lee, P.C., Deisseroth, K., Langston, J.W., Pera, R.R., and Palmer, T.D. (2011). SNCA triplication Parkinson's patient's iPSC-derived DA neurons accumulate alpha-synuclein and are susceptible to oxidative stress. PloS one *6*, e26159.

Castillo-Quan, J.I., Li, L., Kinghorn, K.J., Ivanov, D.K., Tain, L.S., Slack, C., Kerr, F., Nespital, T., Thornton, J., Hardy, J., *et al.* (2016). Lithium Promotes Longevity through GSK3/NRF2-Dependent Hormesis. Cell Rep *15*, 638-650.

Clark, E.H., Vazquez de la Torre, A., Hoshikawa, T., and Briston, T. (2020). Targeting mitophagy in Parkinson's disease. The Journal of biological chemistry.

Consortium, G.T., Laboratory, D.A., Coordinating Center -Analysis Working, G., Statistical Methods groups-Analysis Working, G., Enhancing, G.g., Fund, N.I.H.C., Nih/Nci, Nih/Nhgri, Nih/Nimh, Nih/Nida, *et al.* (2017). Genetic effects on gene expression across human tissues. Nature *550*, 204-213.

Ehrenkaufer, G.M., Suresh, S., Solow-Cordero, D., and Singh, U. (2018). High-Throughput Screening of Entamoeba Identifies Compounds Which Target Both Life Cycle Stages and Which Are Effective Against Metronidazole Resistant Parasites. Front Cell Infect Microbiol *8*, 276.

Hiroyuki Katayama, H.H., Koji Nagasawa, Hiroshi Kurokawa, Mayu Sugiyama, Ryoko Ando,Masaaki Funata, Nobuyo Yoshida, Misaki Homma, Takanori Nishimura, Megumu Takahashi, Yoko Ishida, Hiroyuki Hioki, Yoshiyuki Tsujihata, and Atsushi Miyawaki (2020). Visualizing and Modulating Mitophagy for Therapeutic Studies of Neurodegeneration. Cell *181*, 12.
Hoshino, A., Wang, W.J., Wada, S., McDermott-Roe, C., Evans, C.S., Gosis, B., Morley, M.P., Rathi, K.S., Li, J., Li, K.*, et al.* (2019). The ADP/ATP translocase drives mitophagy independent of nucleotide exchange. Nature *575*, 375-379.
Hsieh, C.H., Li, L., Vanhauwaert, R., Nguyen, K.T., Davis, M.D., Bu, G., Wszolek, Z.K., and Wang, X. (2019). Miro1 Marks Parkinson's Disease Subset and Miro1 Reducer Rescues Neuron Loss in Parkinson's Models. Cell metabolism *30*, 1131-1140 e1137.
Hsieh, C.H., Shaltouki, A., Gonzalez, A.E., Bettencourt da Cruz, A., Burbulla, L.F., St Lawrence, E., Schule, B., Krainc, D., Palmer, T.D., and Wang, X. (2016). Functional Impairment in Miro Degradation and Mitophagy Is a Shared Feature in Familial and Sporadic Parkinson's Disease. Cell stem cell *19*, 709-724.
Kinghorn, K.J., Castillo-Quan, J.I., Bartolome, F., Angelova, P.R., Li, L., Pope, S., Cocheme, H.M., Khan, S., Asghari, S., Bhatia, K.P.*, et al.* (2015). Loss of PLA2G6 leads to elevated mitochondrial lipid peroxidation and mitochondrial dysfunction. Brain : a journal of neurology *138*, 1801-1816.
Kriks, S., Shim, J.W., Piao, J., Ganat, Y.M., Wakeman, D.R., Xie, Z., Carrillo-Reid, L., Auyeung, G., Antonacci, C., Buch, A.*, et al.* (2011). Dopamine neurons derived from human ES cells efficiently engraft in animal models of Parkinson's disease. Nature *480*, 547-551.
Le Guen, Y., Napolioni, V., Belloy, M.E., Yu, E., Krohn, L., Ruskey, J.A., Gan-Or, Z., Kennedy, G., Eger, S.J., and Greicius, M.D. (2021). Common X-Chromosome Variants Are Associated with Parkinson Disease Risk. Ann Neurol *90*, 22-34.
Nalls, M.A., Blauwendraat, C., Vallerga, C.L., Heilbron, K., Bandres-Ciga, S., Chang, D., Tan, M., Kia, D.A., Noyce, A.J., Xue, A.*, et al.* (2019). Identification of novel risk loci, causal insights, and heritable risk for Parkinson's disease: a meta-analysis of genome-wide association studies. The Lancet Neurology *18*, 1091-1102.
Nalls, M.A., Keller, M.F., Hernandez, D.G., Chen, L., Stone, D.J., Singleton, A.B., and Parkinson's Progression Marker Initiative, i. (2016). Baseline genetic associations in the Parkinson's Progression Markers Initiative (PPMI). Movement disorders : official journal of the Movement Disorder Society *31*, 79-85.
Nguyen, H.N., Byers, B., Cord, B., Shcheglovitov, A., Byrne, J., Gujar, P., Kee, K., Schule, B., Dolmetsch, R.E., Langston, W.*, et al.* (2011). LRRK2 mutant iPSC-derived DA neurons demonstrate increased susceptibility to oxidative stress. Cell stem cell *8*, 267-280.
Percha, B., and Altman, R.B. (2018). A global network of biomedical relationships derived from text. Bioinformatics *34*, 2614-2624.
Rentzsch, P., Witten, D., Cooper, G.M., Shendure, J., and Kircher, M. (2019). CADD: predicting the deleteriousness of variants throughout the human genome. Nucleic Acids Res *47*, D886-D894.
Rival, T., Soustelle, L., Strambi, C., Besson, M.T., Iche, M., and Birman, S. (2004). Decreasing glutamate buffering capacity triggers oxidative stress and neuropil degeneration in the Drosophila brain. Current biology : CB *14*, 599-605.
Sanders, L.H., Laganiere, J., Cooper, O., Mak, S.K., Vu, B.J., Huang, Y.A., Paschon, D.E., Vangipuram, M., Sundararajan, R., Urnov, F.D.*, et al.* (2014). LRRK2 mutations cause mitochondrial DNA damage in iPSC-derived neural cells from Parkinson's disease patients: reversal by gene correction. Neurobiology of disease *62*, 381-386.

Shaltouki, A., Hsieh, C.H., Kim, M.J., and Wang, X. (2018). Alpha-synuclein delays mitophagy and targeting Miro rescues neuron loss in Parkinson's models. Acta Neuropathol *136*, 607-620.
Sofola, O., Kerr, F., Rogers, I., Killick, R., Augustin, H., Gandy, C., Allen, M.J., Hardy, J., Lovestone, S., and Partridge, L. (2010). Inhibition of GSK-3 ameliorates Abeta pathology in an adult-onset Drosophila model of Alzheimer's disease. PLoS genetics *6*, e1001087.
Trinh, K., Moore, K., Wes, P.D., Muchowski, P.J., Dey, J., Andrews, L., and Pallanck, L.J. (2008). Induction of the phase II detoxification pathway suppresses neuron loss in Drosophila models of Parkinson's disease. The Journal of neuroscience : the official journal of the Society for Neuroscience *28*, 465-472.
Tsai, P.I., Course, M.M., Lovas, J.R., Hsieh, C.H., Babic, M., Zinsmaier, K.E., and Wang, X. (2014). PINK1-mediated phosphorylation of Miro inhibits synaptic growth and protects dopaminergic neurons in Drosophila. Scientific reports *4*, 6962.
Wichterle, H., Lieberam, I., Porter, J.A., and Jessell, T.M. (2002). Directed differentiation of embryonic stem cells into motor neurons. Cell *110*, 385-397.